

Search for New Physics in the Two Higgs to Four b-quark Final State

by

Alice Cocoros

A dissertation submitted to The Johns Hopkins University
in conformity with the requirements for the degree of
Doctor of Philosophy

Baltimore, Maryland

June, 2017

© Alice Cocoros 2017

All rights reserved

Abstract

My thesis is about bla bla

Primary Reader: Petar Maksimovic

Secondary Reader: Morris Swartz

Acknowledgments

Thanks!

Table of Contents

Abstract	ii
Acknowledgments	iii
1 Introduction	1
1.1 The Standard Model	2
1.1.1 Leptons	5
1.1.2 Quarks	6
1.1.3 Representation of Interactions	7
1.1.4 The Electromagnetic Force:	8
1.1.5 The Strong Force:	9
1.1.6 The Weak Force:	11
1.1.7 Mass and the Higgs Boson	14
1.2 Rounding Up the Standard Model Particles	16
1.3 Beyond the Standard Model	17
2 Introduction	18
2.1 Theoretical overview	18
2.2 Resonant Production	19
2.3 Nonresonant Production	22

3	Searching for New Particles	28
3.1	The Large Hadron Collider	29
3.1.1	A proton-proton Collision	30
3.2	The Compact Muon Solenoid	32
3.2.1	Coordinates	33
3.2.2	The Tracker	35
3.2.3	The Calorimeters	36
3.2.4	The Solenoid	37
3.2.5	The Muon Chambers	37
3.2.6	What's Missing?	38
3.2.7	The Particle Flow Algorithm	39
3.2.8	Jets	40
3.2.9	Triggers	41
3.2.10	Pileup	42
4	Looking for New Physics	44
4.1	Signal Signature	44
4.2	Distinguishing Signal from Background	47
4.2.1	The Soft-Drop Mass Algorithm	47
4.2.2	The N-subjetiness Algorithm	48
4.2.3	B-Tagging	50
4.2.3.1	Deep CSV Algorithm	50
4.2.3.2	Double b Algorithm	51
5	Semi-resolved Analysis	53
5.0.1	Trigger and event cleaning	53

5.0.2	Jet kinematics selection	59
5.0.3	H mass selection	61
5.0.4	Identification of H candidates	65
5.0.4.1	N-subjettiness selection	65
5.0.4.2	Invariant mass definition and “reduced mass” .	68
5.0.5	Boosted and Resolved Selection Rejection	69
5.0.5.1	Boosted Analysis	69
5.0.5.2	Resolved Analysis	72
6	Background Estimate	73
6.0.1	Alphabet Background Estimate	73
6.0.2	Closure Test in Data	75
6.0.3	Signal Regions Prediction	78
7	Statistical Interpretation	89
7.1	Systematic uncertainties	89
8	Conclusion	94
8.1	Results	94
8.2	Results Non resonant	97
8.3	Results	97

List of Tables

2.1	Parameter values of the final benchmarks selected with number of clusters $N_{clus} = 12$	25
8.1	Comparison of semi-boosted (rejecting boosted events) and boosted limits, both expected and observed, for bulk graviton.	97
8.2	Comparison of semi-boosted (rejecting boosted events) and boosted limits, both expected and observed, for radion.	97
8.3	Combined expected and observed limits of boosted and semi- boosted channels for bulk graviton, where the semi-boosted chan- nel retains resolved events but rejects boosted events.	100
8.4	Combined expected and observed limits of boosted and semi- boosted channels for radion, where the semi-boosted channel re- tains resolved events but rejects boosted events.	100
8.5	Comparison of expected limits retaining events from the boosted and resolved selections, rejecting events from the boosted selec- tion, and rejecting events from the boosted and resolved selec- tions for bulk graviton.	100

8.6 Comparison of expected limits retaining events from the boosted and resolved selections, rejecting events from the boosted selec- tion, and rejecting events from the boosted and resolved selec- tions for radion.	101
--	-----

List of Figures

1.1	Snapshot of a cloud chamber, circa 1933: the vertical line represents a positron traveling through the cloud chamber, curving due to the magnetic field applied to the chamber.	1
1.2	The Standard Model Lagrangian.	3
1.3	Table of Standard Model particles. Image from CERN [1]. . . .	4
1.4	Visual representation of the interaction between two electrons (straight lines) and a photon (wavy line).	7
1.5	A Feynman Diagram showing the interaction of two electrons. Time increases to the right on the x-axis, and the y-axis represents the distance between the two electrons.	8
1.6	A Feynman Diagram showing the annihilation of a positron and an electron.	9
1.7	QCD interactions can be described by three vertices. The curly line represents gluons, while the straight lines represent quarks. Since gluons are colored, they can interact with themselves. . . .	10

1.8 Weak interactions can be described by the following vertices. The wavy lines represent bosons, while the straight lines represent any weak-interacting particle where the appropriate quantities are conserved.	12
1.9 Approximation of the Higgs potential. While the shape is symmetric about the y-axis, the function is not symmetric about the minima.	14
1.10 The Higgs Vertex. The dashed line is the Higgs Boson and the straight lines are any massive particle.	15
1.11 Left: Two gluons interact with a quark, while each gluon interacts with an additional different quark, and these additional different quarks interact with a shared fourth quark and each pair of quarks interacts to form a Higgs boson. Right: Two gluons interact with a quark, while each gluon interacts with an additional quark, and these additional different quarks interact with each other to form a Higgs boson, which interacts with two Higgs bosons. The result of both of these processes is a final state with two Higgs.	16
2.1 A depiction of the fifth extra dimension.	20
2.2 SM Feynman diagrams that contribute to Higgs boson pair production by gluon-gluon fusion at leading order.	22

2.3	SM Feynman diagrams that contribute to Higgs boson pair production by gluon-gluon fusion at leading order. Diagrams (a) and (b) correspond to SM-like processes, while diagrams (c), (d), and (e) correspond to pure BSM effects: (c) and (d) describe contact interactions between the Higgs boson and gluons, and (e) exploits the contact interaction of two Higgs bosons with top quarks.	24
2.4	The invariant mass of the two Higgs for Monte Carlo simulation of different parameter combinations, clustered into 12 classes of shapes. The red distributions correspond to the benchmark model, while the blue distributions are the other parameter combinations similar to the benchmark that are part of that cluster.	26
2.5	The modulus of the cosine of the polar angle of one Higgs boson with respect to the beam axis for Monte Carlo simulation of different parameter combinations, clustered into 12 classes of shapes. The red distributions correspond to the benchmark model, while the blue distributions are the other parameter combinations similar to the benchmark that are part of that cluster.	27
3.1	(left) Schematic of the LHC and the smaller accelerators which feed into the LHC. (right) Aerial view of Geneva. The larger circle marks the location of the LHC, safely underneath the ground.	29
3.2	PDF for 10 GeV (left) and 10 TeV (right) collisions. Each curve represents a parton in a proton, and tells us the probability (y-axis) of finding that parton carrying momentum fraction x of the total momentum of the proton.	31

3.3	The Compact Muon Solenoid detector.	32
3.4	CMS detector with a person for size (top). Slice of the CMS detector, depicting the different components and the signatures of some of the different particles that pass through the detector after a proton-proton collision occurs (bottom).	34
3.5	Coordinates of the CMS detector.	35
3.6	Diagram of particles inside the detector pre-collision (top) and post-collision (bottom), where post-collision shows where the protons entered, which particles were recorded (blue), and the direction of the missing energy (orange).	39
3.7	Typical CMS event with large number of hadrons (tracks represented by green lines, HCAL energy in blue, ECAL energy in red). These hadrons are collected into <i>jets</i> (shown by yellow triangles). The PF algorithm combines information from the trackers and calorimeters to properly measure the total momentum and energy of the jet.	40
4.1	Drawing of decay products with varying degrees of Lorentz boost.	45
4.2	Signature for resolved two Higgs to four b-quarks.	46
4.3	Signature for merged two Higgs to four b-quarks.	46
4.4	The mass of ungroomed jets (left) is a poor choice for differentiating jets from real top decays. The Soft Drop algorithm (right) allows the W and top peaks to be identified and reduces the mass of most background jets. The peak around 100 GeV is the W, while the peak around 200 is the top.	49

4.5	N-subjetness variable τ_3/τ_2 for top jets and background jets. A cut can be made that keeps only jets with low values of τ_3/τ_2 , thus reducing the background.	50
4.6	CSV (version 2) discriminator for jets from a light (dashed line), charm (dotted line) and b (solid line) partons. The discriminator peaks sharply at 1 for jets originating from a b parton.	52
5.1	The trigger efficiency, as a function of $M_{\text{jjj}}^{\text{red}} \equiv M_{\text{jjj}} - (M_{\text{jet}}^1 - M_{\text{H}}) - (M_{\text{jet}}^2 - M_{\text{H}})$, defined in Section 5.0.4.2, in the data and QCD MC, where M_{jet}^1 is the AK8 softdrop mass, M_{jet}^2 is the combined AK4 dijetmass, and M_{H} is 125. Efficiency is defined for different $\Delta\eta$ regions: 0.0–1.0 (left), 1.0–2.0 (right). The 23Sep2016 re-reco for Runs2016B-G and PromptReco for Run2016H are used, totalling to an integrated luminosity of 35.9.	56
5.2	The trigger efficiency for the baseline trigger HLT_PFT260, as a function of $M_{\text{jjj}}^{\text{red}} \equiv M_{\text{jjj}} - (M_{\text{jet}}^1 - M_{\text{H}}) - (M_{\text{jet}}^2 - M_{\text{H}})$, defined in Section 5.0.4.2, for different $\Delta\eta$ regions: 0.0–1.0 (left) and 1.0–2.0 (right). The percentage difference between one and these turn-on curves are taken as an uncertainty on the trigger efficiency scale factor.	57
5.3	The trigger efficiency scale factors, as a function of $M_{\text{jjj}}^{\text{red}}$, defined in Section 5.0.4.2. The error bars are the combined statistical and systematic errors. The 23Sep2016 re-reco for Runs2016B-G and PromptReco for Run2016H are used, totalling to an integrated luminosity of 35.9.	58

5.4	Left.	The <i>of the AK8 jet. Right. The</i>
		η of the AK8 jet. 62
5.5	Left.	The <i>of the highest</i>
		selected AK4 jet. Right. The η of the highest <i>selected AK4 jet.</i>
	 62
5.6	Left.	The <i>of the other selected AK4 jet. Right. The</i>
		η of the other selected AK4 jet. 62
5.7		The absolute value of $\Delta\eta$ between the AK8 jet and the combined 4 vector of the AK4 jets. We require $ \Delta\eta < 2.0$ 63
5.8		The soft-drop mass of the AK8 jet. We require it to be between 105 and 135 GeV. 64
5.9		The dijet mass of the AK4 jet. We require it to be between 90 and 140 GeV. 64
5.10		τ_{21} distribution for the AK8 jet. We require $\tau_{21} < 0.55$ 65
5.11		Double-b tagger discriminant for the AK8 jet. We require double b tagger > 0.8 67

5.12 Deep CSV P(b) + P(bb) tagger discriminant for the highest selectedAK4jet(left)andtheotherselectedAK4jet(right).WerequireddeepCSV >0.6324	68
5.13 TriAk4jet mass: the invariant mass of the two selected AK4 jets and the nearest unselected AK4 jet. We require triAK4jet mass > 200 GeV.	69
5.14 Reduced mass of the two selected AK4 jets and the AK8 jet.	70
6.1 Schematic representation of the regions used to perform our es- timate.	74
6.2 First control region (AK4 dijet mass < 70 GeV and remove the triAK4jet mass requirement) (left) Fits in the mass sideband regions for the conversion rates $R_{p/f}$ for a selection rejecting boosted events.(right) Application of those fits to the anti-tag region to estimate the background in the first control regions, compared with the true background (black markers). Top is $\Delta\eta$ 0 - 1.0 and bottom is $\Delta\eta$ 1.0 - 2.0.	76
6.3 Second control region (AK4 jet 2 deep CSV < 0.6324 and remove the triAK4jet mass requirement). (left) Fits in the mass side- band regions for the conversion rates $R_{p/f}$ for a selection rejecting boosted events.(right) Application of those fits to the anti-tag re- gion to estimate the background in the control regions, compared with the true background (black markers). Top is $\Delta\eta$ 0 - 1.0 and bottom is $\Delta\eta$ 1.0 - 2.0.	77

6.4 First control region. (left) Fits in the mass sideband regions for the conversion rates $R_{p/f}$ for a selection retaining both boosted and resolved events.(right) Application of those fits to the anti-tag region to estimate the background in the control regions, compared with the true background (black markers). Top is $\Delta\eta$ 0 - 1.0 and bottom is $\Delta\eta$ 1.0 - 2.0.	78
6.5 Second control region. (left) Fits in the mass sideband regions for the conversion rates $R_{p/f}$ for a selection retaining both boosted and resolved events.(right) Application of those fits to the anti-tag region to estimate the background in the control regions, compared with the true background (black markers). Top is $\Delta\eta$ 0 - 1.0 and bottom is $\Delta\eta$ 1.0 - 2.0.	79
6.6 First control region. (left) Fits in the mass sideband regions for the conversion rates $R_{p/f}$ for a selection rejecting both boosted and resolved events.(right) Application of those fits to the anti-tag region to estimate the background in the control regions, compared with the true background (black markers). Top is $\Delta\eta$ 0 - 1.0 and bottom is $\Delta\eta$ 1.0 - 2.0.	80
6.7 Second control region. (left) Fits in the mass sideband regions for the conversion rates $R_{p/f}$ for a selection rejecting both boosted and resolved events.(right) Application of those fits to the anti-tag region to estimate the background in the control regions, compared with the true background (black markers). Top is $\Delta\eta$ 0 - 1.0 and bottom is $\Delta\eta$ 1.0 - 2.0.	81

6.8 (left) Fits in the mass sideband regions for the conversion rates $R_{p/f}$ for a selection rejecting boosted events.(right) Application of those fits to the anti-tag region to estimate the background in the first control regions, compared with the true background (black markers). Top is $\Delta\eta$ 0 - 1.0 and bottom is $\Delta\eta$ 1.0 - 2.0.	82
6.9 (left) Fits in the mass sideband regions for the conversion rates $R_{p/f}$ for a selection retaining both boosted and resolved events.(right) Application of those fits to the anti-tag region to estimate the background in the control regions, compared with the true background (black markers). Top is $\Delta\eta$ 0 - 1.0 and bottom is $\Delta\eta$ 1.0 - 2.0.	83
6.10 (left) Fits in the mass sideband regions for the conversion rates $R_{p/f}$ for a selection rejecting both boosted and resolved events.(right) Application of those fits to the anti-tag region to estimate the background in the control regions, compared with the true background (black markers). Top is $\Delta\eta$ 0 - 1.0 and bottom is $\Delta\eta$ 1.0 - 2.0.	84
6.11 (left) Fits in the mass sideband regions for the conversion rates $R_{p/f}$ for a selection rejecting boosted events.(right) Application of those fits to the anti-tag region to estimate the background in the unblinded signal region. Top is $\Delta\eta$ 0 - 1.0 and bottom is $\Delta\eta$ 1.0 - 2.0.	85

6.12 (left) Fits in the mass sideband regions for the conversion rates $R_{p/f}$ for a selection rejecting boosted and resolved events.(right) Application of those fits to the anti-tag region to estimate the background in the unblinded signal region. Top is $\Delta\eta$ 0 - 1.0 and bottom is $\Delta\eta$ 1.0 - 2.0.	86
6.13 (left) Fits in the mass sideband regions for the conversion rates $R_{p/f}$ for a selection retaining boosted and resolved events.(right) Application of those fits to the anti-tag region to estimate the background in the unblinded signal region. Top is $\Delta\eta$ 0 - 1.0 and bottom is $\Delta\eta$ 1.0 - 2.0.	87
6.14 The difference in rejecting only boosted signal region events versus rejecting any boosted event used for background estimate, as can be seen in the $\Delta\eta$ 0-1 region (top) and 1-2 region (bottom).	88
7.1 Datacard for Bulk Graviton 1000 GeV rejecting boosted events for $\Delta\eta$ 0-1.	93
8.1 Blinded limits for bulk graviton for the selection rejecting boosted events.	95
8.2 Blinded limits for radion for the selection rejecting boosted events.	96
8.3 Unblinded limits for bulk graviton for the selection rejecting boosted events, combining boosted selection and semi-boosted selection.	98
8.4 Unblinded limits for radion for the selection rejecting boosted events, combining boosted selection and semi-boosted selection.	99
8.5 Blinded limits for bulk graviton for the selection rejecting boosted and resolved events.	101

8.6	Blinded limits for bulk graviton for the selection retaining boosted and resolved events.	102
8.7	Blinded limits for radion for the selection rejecting boosted and resolved events.	103
8.8	Blinded limits for radion for the selection retaining boosted and resolved events.	104
8.9	Bulk graviton (left) and radion (right) limits for all three channels, resolved (green), semi-boosted (aqua), boosted (royal blue), where no channel rejects the events of another channel.	104
8.10	The expected limits for the full selection + boosted rejection, full selection + boosted + resolved rejection, and full selection for bulk graviton (left) and radion (right).	105
8.11	Non-resonant limits for all three channels, resolved (green), semi-boosted (aqua), boosted (royal blue), where no channel rejects the events of another channel. SM = 0 and v1 benchmarks are 1-12.	105

Chapter 1

Introduction

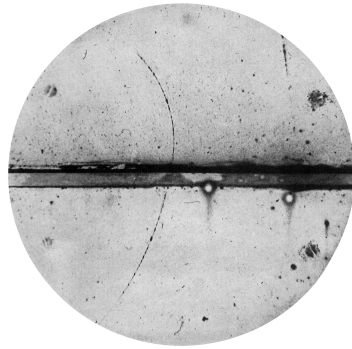


Figure 1.1: Snapshot of a cloud chamber, circa 1933: the vertical line represents a positron traveling through the cloud chamber, curving due to the magnetic field applied to the chamber.

In 1869, Johann Wilhelm Hittorf discovered cathode rays[2], suggesting that there may be subatomic particles. By 1911, these were identified as electrons, observed in many different ways, including cloud chambers, as can be seen in Figure 1.1. Soon after, protons were discovered in 1917, followed by neutrons in 1935.

As physicists advanced the study of quantum mechanics, many new particles were discovered. These particles can be broken down into several elementary particles, whose interactions are governed by *The Standard Model* (SM).

1.1 The Standard Model

The SM describes the interaction of all elementary particles with one formula, shown in Figure 1.2. This lengthy Lagrangian can be summarized as a list of particles and mediating forces, represented in Figure 1.3.

$$\begin{aligned}
& -\frac{1}{2}\partial_\nu g_\mu^a \partial_\nu g_\mu^a - g_s f^{abc} \partial_\mu g_\nu^a g_\mu^b g_\nu^c - \frac{1}{4}g_s^2 f^{abc} f^{ade} g_\mu^b g_\nu^c g_\mu^d g_\nu^e + \\
& \frac{1}{2}ig_s^2 (\bar{q}_i^\sigma \gamma^\mu q_j^\sigma) g_\mu^a + \bar{G}^a \partial^2 G^a + g_s f^{abc} \partial_\mu \bar{G}^a G^b g_\mu^c - \partial_\nu W_\mu^+ \partial_\nu W_\mu^- - \\
& M^2 W_\mu^+ W_\mu^- - \frac{1}{2} \partial_\nu Z_\mu^0 \partial_\nu Z_\mu^0 - \frac{1}{2c_w^2} M^2 Z_\mu^0 Z_\mu^0 - \frac{1}{2} \partial_\mu A_\nu \partial_\mu A_\nu - \frac{1}{2} \partial_\mu H \partial_\mu H - \\
& \frac{1}{2} m_h^2 H^2 - \partial_\mu \phi^+ \partial_\mu \phi^- - M^2 \phi^+ \phi^- - \frac{1}{2} \partial_\mu \phi^0 \partial_\mu \phi^0 - \frac{1}{2c_w^2} M \phi^0 \phi^0 - \beta_h [\frac{2M^2}{g^2} + \\
& \frac{2M}{g} H + \frac{1}{2}(H^2 + \phi^0 \phi^0 + 2\phi^+ \phi^-)] + \frac{2M^4}{g^2} \alpha_h - ig c_w [\partial_\nu Z_\mu^0 (W_\mu^+ W_\nu^- - \\
& W_\nu^+ W_\mu^-) - Z_\mu^0 (W_\mu^+ \partial_\nu W_\mu^- - W_\mu^- \partial_\nu W_\mu^+) + Z_\mu^0 (W_\nu^+ \partial_\nu W_\mu^- - \\
& W_\nu^- \partial_\nu W_\mu^+)] - ig s_w [\partial_\nu A_\mu (W_\mu^+ W_\nu^- - W_\nu^+ W_\mu^-) - A_\nu (W_\mu^+ \partial_\nu W_\mu^- - \\
& W_\mu^- \partial_\nu W_\mu^+) + A_\mu (W_\nu^+ \partial_\nu W_\mu^- - W_\nu^- \partial_\nu W_\mu^+)] - \frac{1}{2} g^2 W_\mu^+ W_\nu^- W_\mu^+ W_\nu^- + \\
& \frac{1}{2} g^2 W_\mu^+ W_\nu^- W_\mu^+ W_\nu^- + g^2 c_w^2 (Z_\mu^0 W_\mu^+ Z_\nu^0 W_\nu^- - Z_\mu^0 Z_\mu^0 W_\nu^+ W_\nu^-) + \\
& g^2 s_w^2 (A_\mu W_\mu^+ A_\nu W_\nu^- - A_\mu A_\nu W_\mu^+ W_\nu^-) + g^2 s_w c_w [A_\mu Z_\nu^0 (W_\mu^+ W_\nu^- - \\
& W_\nu^+ W_\mu^-) - 2A_\mu Z_\mu^0 W_\nu^+ W_\nu^-] - g\alpha [H^3 + H\phi^0 \phi^0 + 2H\phi^+ \phi^-] - \\
& \frac{1}{8} g^2 \alpha_h [H^4 + (\phi^0)^4 + 4(\phi^+ \phi^-)^2 + 4(\phi^0)^2 \phi^+ \phi^- + 4H^2 \phi^+ \phi^- + 2(\phi^0)^2 H^2] - \\
& g M W_\mu^+ W_\mu^- H - \frac{1}{2} g \frac{M}{c_w^2} Z_\mu^0 H - \frac{1}{2} g [W_\mu^+ (\phi^0 \partial_\mu \phi^- - \phi^- \partial_\mu \phi^0) - \\
& W_\mu^- (\phi^0 \partial_\mu \phi^+ - \phi^+ \partial_\mu \phi^0)] + \frac{1}{2} g [W_\mu^+ (H \partial_\mu \phi^- - \phi^- \partial_\mu H) - W_\mu^- (H \partial_\mu \phi^+ - \\
& \phi^+ \partial_\mu H)] + \frac{1}{2} g \frac{1}{c_w} (Z_\mu^0 (H \partial_\mu \phi^0 - \phi^0 \partial_\mu H) - ig \frac{s_w^2}{c_w} M Z_\mu^0 (W_\mu^+ \phi^- - W_\mu^- \phi^+) + \\
& ig s_w M A_\mu (W_\mu^+ \phi^- - W_\mu^- \phi^+) - ig \frac{1-2c_w^2}{2c_w} Z_\mu^0 (\phi^+ \partial_\mu \phi^- - \phi^- \partial_\mu \phi^+) + \\
& ig s_w A_\mu (\phi^+ \partial_\mu \phi^- - \phi^- \partial_\mu \phi^+) - \frac{1}{4} g^2 W_\mu^+ W_\mu^- [H^2 + (\phi^0)^2 + 2\phi^+ \phi^-] - \\
& \frac{1}{4} g^2 \frac{1}{c_w} Z_\mu^0 Z_\mu^0 [H^2 + (\phi^0)^2 + 2(2s_w^2 - 1)^2 \phi^+ \phi^-] - \frac{1}{2} g^2 \frac{s_w^2}{c_w} Z_\mu^0 \phi^0 (W_\mu^+ \phi^- + \\
& W_\mu^- \phi^+) - \frac{1}{2} ig^2 \frac{s_w^2}{c_w} Z_\mu^0 H (W_\mu^+ \phi^- - W_\mu^- \phi^+) + \frac{1}{2} g^2 s_w A_\mu \phi^0 (W_\mu^+ \phi^- + \\
& W_\mu^- \phi^+) + \frac{1}{2} ig^2 s_w A_\mu H (W_\mu^+ \phi^- - W_\mu^- \phi^+) - g^2 \frac{s_w}{c_w} (2c_w^2 - 1) Z_\mu^0 A_\mu \phi^+ \phi^- - \\
& g^1 s_w^2 A_\mu A_\mu \phi^+ \phi^- - \bar{e}^\lambda (\gamma \partial + m_e^\lambda) e^\lambda - \bar{\nu}^\lambda \gamma \partial u^\lambda - \bar{u}_j^\lambda (\gamma \partial + m_u^\lambda) u_j^\lambda - \\
& d_j^\lambda (\gamma \partial + m_d^\lambda) d_j^\lambda + ig s_w A_\mu [-(\bar{e}^\lambda \gamma^\mu e^\lambda) + \frac{2}{3} (\bar{u}_j^\lambda \gamma^\mu u_j^\lambda) - \frac{1}{3} (\bar{d}_j^\lambda \gamma^\mu d_j^\lambda)] + \\
& \frac{ig}{4c_w} Z_\mu^0 [(\bar{\nu}^\lambda \gamma^\mu (1 + \gamma^5) \nu^\lambda) + (\bar{e}^\lambda \gamma^\mu (4s_w^2 - 1 - \gamma^5) e^\lambda) + (\bar{u}_j^\lambda \gamma^\mu (\frac{4}{3} s_w^2 - \\
& 1 - \gamma^5) u_j^\lambda) + (\bar{d}_j^\lambda \gamma^\mu (1 - \frac{8}{3} s_w^2 - \gamma^5) d_j^\lambda)] + \frac{ig}{2\sqrt{2}} W_\mu^+ [(\bar{\nu}^\lambda \gamma^\mu (1 + \gamma^5) e^\lambda) + \\
& (\bar{u}_j^\lambda \gamma^\mu (1 + \gamma^5) C_{\lambda\kappa} d_j^\kappa)] + \frac{ig}{2\sqrt{2}} W_\mu^- [(\bar{e}^\lambda \gamma^\mu (1 + \gamma^5) \nu^\lambda) + (d_j^\kappa C_{\lambda\kappa}^\dagger \gamma^\mu (1 + \\
& \gamma^5) u_j^\lambda)] + \frac{ig}{2\sqrt{2}} \frac{m_e^\lambda}{M} [-\phi^+ (\bar{\nu}^\lambda (1 - \gamma^5) e^\lambda) + \phi^- (\bar{e}^\lambda (1 + \gamma^5) \nu^\lambda)] - \\
& \frac{g}{2} \frac{m_e^\lambda}{M} [H(\bar{e}^\lambda e^\lambda) + i\phi^0 (\bar{e}^\lambda \gamma^5 e^\lambda)] + \frac{-ig}{2M\sqrt{2}} \phi^+ [-m_d^\kappa (\bar{u}_j^\lambda C_{\lambda\kappa} (1 - \gamma^5) d_j^\kappa)] + \\
& m_u^\lambda (\bar{u}_j^\lambda C_{\lambda\kappa} (1 + \gamma^5) d_j^\kappa) + \frac{ig}{2M\sqrt{2}} \phi^- [m_d^\lambda (\bar{d}_j^\lambda C_{\lambda\kappa}^\dagger (1 + \gamma^5) u_j^\kappa) - m_u^\kappa (\bar{d}_j^\lambda C_{\lambda\kappa}^\dagger (1 - \\
& \gamma^5) u_j^\kappa)] - \frac{g}{2} \frac{m_u^\lambda}{M} H (\bar{u}_j^\lambda u_j^\lambda) - \frac{g}{2} \frac{m_d^\lambda}{M} H (\bar{d}_j^\lambda d_j^\lambda) + \frac{ig}{2} \frac{m_u^\lambda}{M} \phi^0 (\bar{u}_j^\lambda \gamma^5 u_j^\lambda) - \\
& \frac{ig}{2} \frac{m_d^\lambda}{M} \phi^0 (\bar{d}_j^\lambda \gamma^5 d_j^\lambda) + \bar{X}^+ (\partial^2 - M^2) X^+ + \bar{X}^- (\partial^2 - M^2) X^- + \bar{X}^0 (\partial^2 - \\
& M^2) X^0 + \bar{Y} \partial^2 Y + ig c_w W_\mu^+ (\partial_\mu \bar{X}^0 X^- - \partial_\mu \bar{X}^+ X^0) + ig s_w W_\mu^+ (\partial_\mu \bar{Y} X^- - \\
& \partial_\mu \bar{X}^+ Y) + ig c_w W_\mu^- (\partial_\mu \bar{X}^- X^0 - \partial_\mu \bar{X}^0 X^+) + ig s_w W_\mu^- (\partial_\mu \bar{X}^- Y - \\
& \partial_\mu \bar{Y} X^+) + ig c_w Z_\mu^0 (\partial_\mu \bar{X}^+ X^+ - \partial_\mu \bar{X}^- X^-) + ig s_w A_\mu (\partial_\mu \bar{X}^+ X^+ - \\
& \partial_\mu \bar{X}^- X^-) - \frac{1}{2} g M [\bar{X}^+ X^+ H + \bar{X}^- X^- H + \frac{1}{c_w^2} \bar{X}^0 X^0 H] + \\
& \frac{1-2c_w^2}{2c_w} ig M [\bar{X}^+ X^0 \phi^+ - \bar{X}^- X^0 \phi^-] + \frac{1}{2c_w^2} ig M [\bar{X}^0 X^- \phi^+ - \bar{X}^0 X^+ \phi^-] + \\
& ig M s_w [\bar{X}^0 X^- \phi^+ - \bar{X}^0 X^+ \phi^-] + \frac{1}{2} ig M [\bar{X}^+ X^+ \phi^0 - \bar{X}^- X^- \phi^0]
\end{aligned}$$

Figure 1.2: The Standard Model Lagrangian.

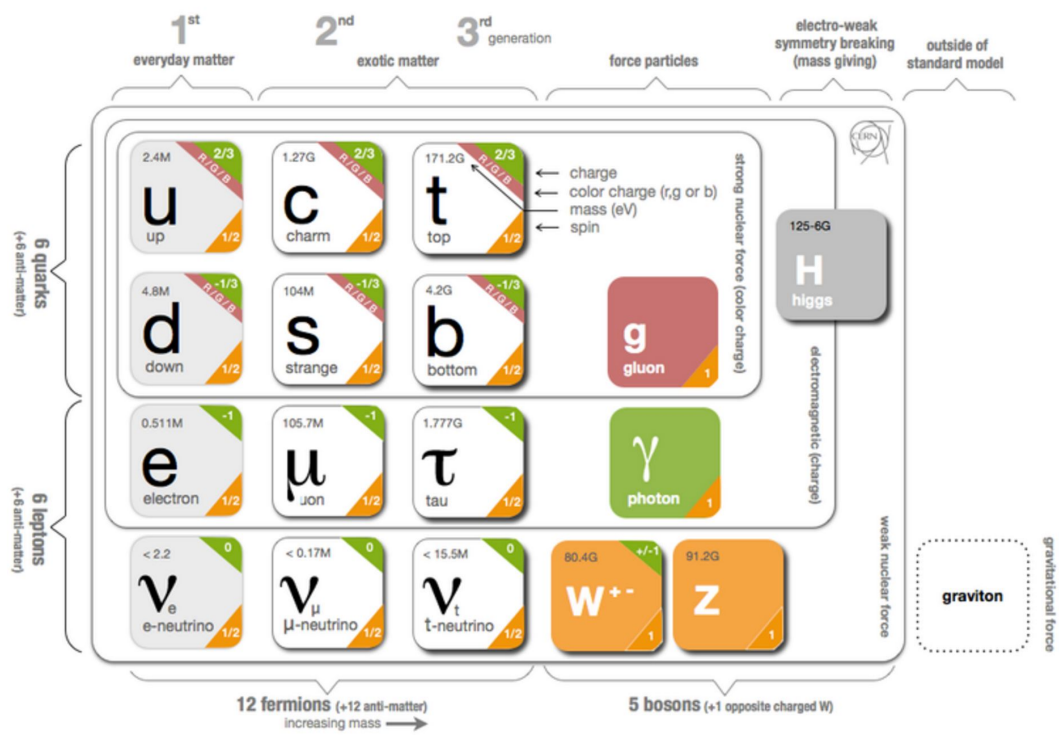


Figure 1.3: Table of Standard Model particles. Image from CERN [1].

1.1.1 Leptons

The electron is one of the most well known elementary particles. There exist two heavier “versions” of the electron: the muon (μ) which is ~ 200 times as massive as the electron, and the tau (τ) which is ~ 4000 times as massive as the electron. Each of these particles is negatively charged, where the charge is equivalent to -1 which corresponds to -1.602×10^{-19} Coulombs.

For each of these particles, there exists a corresponding neutrino: the electron ν_e , the muon neutrino ν_μ , and the tau neutrino ν_τ . The neutrinos as defined by the SM are chargeless and massless, although experiments have proved that at least two out of three neutrinos observed in nature have mass. The electron and its corresponding neutrino are first generation fermions, while the muon and its neutrino are second generation and the tau and its neutrino are third generation.

A corresponding anti-particle exists for each of these six particles: \bar{e} (e^+), $\bar{\mu}$ (μ^+), $\bar{\tau}$ (τ^+), $\bar{\nu}_e$, $\bar{\nu}_\mu$, and $\bar{\nu}_\tau$. Note that, while neutrinos are chargeless, the anti-particle for the electron, muon, and tau, all have positive (or opposite of their corresponding particle) charge. However, each anti-particle is identical in mass to its corresponding particle.

In addition to charge and mass, particles also have spin, or the intrinsic angular momentum of a particle. All of the above mentioned particles, known as leptons, have spin $\frac{1}{2}$ (or $-\frac{1}{2}$), which means they are fermions. The spin of a particle allows us to define helicity, also known as handedness. This is the sign of the projection of the particle’s spin vector onto its momentum vector.

A particle is said to be right-handed if the spin and momentum align, and left-handed if the spin and momentum point opposite each other. In the Standard Model, there can be difference between left-handed and right-handed particles. For example, we have observed that all neutrinos are left-handed, while all anti-neutrinos are right-handed, which is currently still inexplicable.

1.1.2 Quarks

Many of the particles discovered in the twentieth century are composite particles called hadrons, made up of quarks. There are six quarks: *up* (*u*) and *down* (*d*) (first generation), *strange* (*s*) and *charm* (*c*) (second generation), and *bottom* (*b*) and *top* (*t*) (third generation).

The *u*, *c* and *t* quarks have charge $+\frac{2}{3}$ and the *d*, *s* and *b* quarks have charge $-\frac{1}{3}$. Quarks also have each a different mass. For every quark there is an anti-quark (\bar{u} , \bar{d} , \bar{s}, \bar{c} , \bar{b} and \bar{t}) with an opposite charge. Quarks are also fermions, and therefore have a spin of $\frac{1}{2}$ or $-\frac{1}{2}$.

In addition to charge (by which we mean electric charge), mass, and spin, quarks also have a second kind of charge, known as color. While electric charge allows particles to interact through the electromagnetic force, color charge allows particles to interact through a different type of force, called the strong force. Quarks can be red, green, or blue colored, and anti-quarks can be anti-red, anti-green, or anti-blue colored. In nature, we only see color neutral particles, which is why quarks are only observed as combinations forming composite particles. These composite particles made up of quarks are color neutral because they either contain one quark of each color, or a quark of a particular color and a quark of the corresponding anti-color. For example, the proton is made up of

one u and two d quarks, so one of these must be red, one must be green, and one must be blue.

1.1.3 Representation of Interactions

The Standard Model describes how matter particles, described above, interact with each other through the exchange of force mediating particles. Each term in the Lagrangian in Figure 1.2 represents different types of interactions between particles. Let us consider a simple scenario of electron electron interaction, which happens through the exchange of the electromagnetic mediating particle known as the photon. Instead of considering the mathematical term associated with this process, it is easier to draw the actual interaction using a vertex, as can be seen in Figure 1.4. This vertex can be arranged and combined with

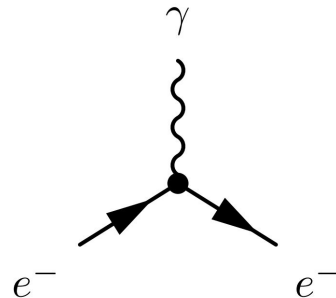


Figure 1.4: Visual representation of the interaction between two electrons (e^-) and a photon (γ).

other vertices in a variety of ways to represent different interactions between electrons, positrons, and photons. For example, we can consider the case where two electrons are propelled towards each other. Using two of the vertex pictured in 1.4, we can see that this must result in two electrons, as can be seen in Figure 1.5, where time propagates to the right on the x-axis, and distance is represented

on the y-axis. Alternatively, if we were to consider the interaction between an

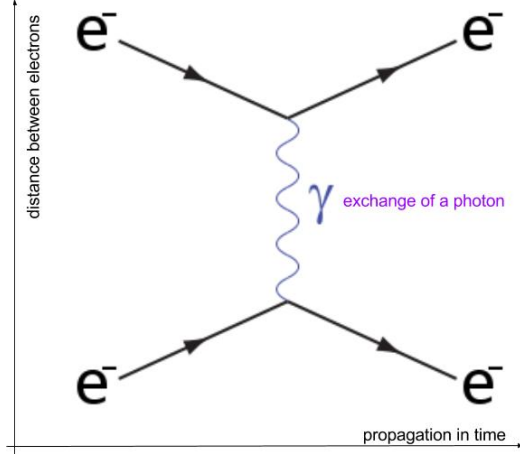


Figure 1.5: A Feynman Diagram showing the interaction of two electrons. Time increases to the right on the x-axis, and the y-axis represents the distance between the two electrons.

electron and a positron, which can be represented as an electron with an arrow pointing backwards in time, we can see that the resulting process is described by Figure 1.6, where an electron and a positron annihilate to a photon, which produces an electron positron pair. In both of these diagrams, we notice that charge is conserved on either side of the diagram. Many more diagrams can be made with this vertex, combining it with other vertices that involve a photon or electrons as well. In understanding diagrams like these, we can explain three of the four fundamental forces at a qualitative level, below, while also introducing new theories in later chapters that have motivated the search for new particles.

1.1.4 The Electromagnetic Force:

Quantum electrodynamics (QED) describes how the electromagnetic force behaves at the quantum level. The force carrier of QED is the photon, γ , which is

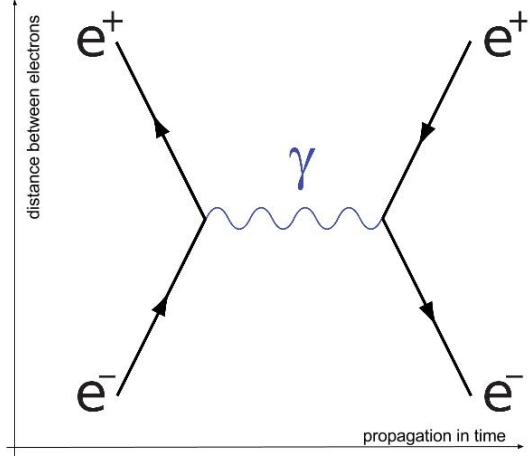


Figure 1.6: A Feynman Diagram showing the annihilation of a positron and an electron.

massless and moves at the speed of light. This theory can be described by diagrams like Figure 1.4, where any fermion with an electric charge can replace the electron. It should be noted that since the photon has neutral electric charge, it cannot couple to itself, and these diagrams with two electrically charged fermions and one photon represent the theory in full. Many experiments have performed precision measurements of QED properties, verifying that they match SM predictions extremely well.

1.1.5 The Strong Force:

Quantum Chromodynamics (QCD) describes quantum interactions related to the strong force. The force carrier of QCD is the gluon, g , which is massless and moves at the speed of light. The gluon does have color charge, just as the quarks do, and therefore there are a number of vertices in QCD, as shown in Figure 1.7. As mentioned before, each quark has a color charge, and each anti-quark has an anti-color charge. Since color must be conserved, we can see

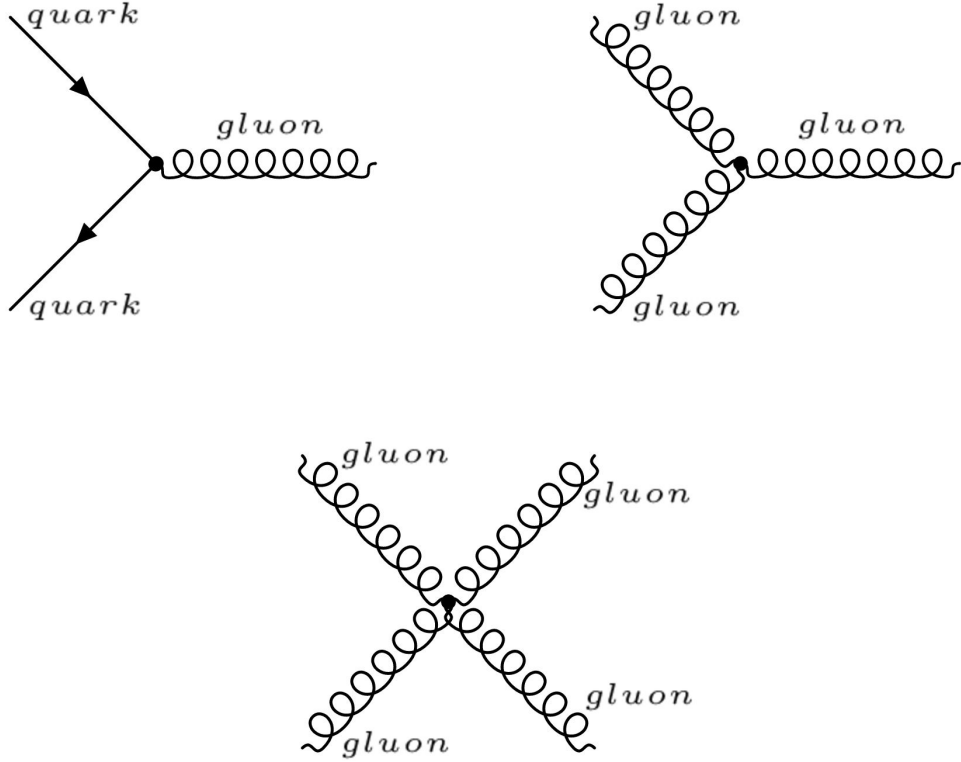


Figure 1.7: QCD interactions can be described by three vertices. The curly line represents gluons, while the straight lines represent quarks. Since gluons are colored, they can interact with themselves.

that the gluon must carry a color and an anti-color for the vertices in Figure 1.7 to be true. Naively, since there are three colors, one would think there are nine gluons, or nine possible combination of three colors and three anticolors. These are summarized below:

$$\begin{array}{cccc}
 \frac{r\bar{r}+b\bar{b}+g\bar{g}}{\sqrt{3}} & & & \\
 \frac{r\bar{b}+b\bar{r}}{\sqrt{2}} & \frac{r\bar{g}+g\bar{r}}{\sqrt{2}} & \frac{b\bar{g}+g\bar{b}}{\sqrt{2}} & \frac{r\bar{r}-b\bar{b}}{\sqrt{2}} \\
 \frac{-i(r\bar{b}-b\bar{r})}{\sqrt{2}} & \frac{-i(r\bar{g}-g\bar{r})}{\sqrt{2}} & \frac{-i(b\bar{g}-g\bar{b})}{\sqrt{2}} & \frac{r\bar{r}+b\bar{b}-2g\bar{g}}{\sqrt{6}}
 \end{array}$$

Both mesons (two-quark bound states) and baryons (three-quark bound states) must be color neutral. We know that a particle can be neutral if it

contains either quarks with color-anti-color, or all three color quarks. Then since the combination of red, green, and blue is neutral, the first combination listed, $\frac{r\bar{r}+b\bar{b}+g\bar{g}}{\sqrt{3}}$, would be color neutral. However, color neutral particles must be non-interacting, otherwise colorless baryons would emit these gluons and interact with one another through the strong force, which we do not observe in nature. Therefore, this first combination is not possible, and there are only eight gluons, called the color octet.

The strong force is responsible for hadronization, or the production of many quarks and gluons when quarks are smashed apart due to an event such as a proton-proton collision. As quarks drift apart after the collision, a color tube of self-interacting gluons is created between the quarks. These tubes are stretched as the quarks drift further apart, increasing energy in the tube due to the constant force exerted from stretching. At distances of roughly 10^{-15} m, it becomes more energetically favorable for two new quarks to be created from the vacuum, through the process shown in the top left vertex in Figure 1.7. If these new quarks are still too energetic to be contained in a particle, this process will repeat until the energy has been sufficiently decreased for all new quark pairs to stay bound. This property is known as confinement, and is critical to the understanding of hadronic activity within a particle detector.

1.1.6 The Weak Force:

When the universe had first begun and was still very hot, the weak force and the electromagnetic force were combined to form the electroweak force. At this time, the electroweak interaction was mediated by four massless bosons: W_1 , W_2 , W_3 and B . As the universe cooled, the bosons eventually began interacting

with the Higgs field (addressed in the following section), and soon, the bosons that interacted with fermions were no longer these four, but a superposition of them. We can write this superpositions as

$$\begin{pmatrix} \gamma \\ Z \end{pmatrix} = \begin{pmatrix} \cos \theta_W & \sin \theta_W \\ -\sin \theta_W & \cos \theta_W \end{pmatrix} \begin{pmatrix} B \\ W_3 \end{pmatrix} \quad (1.1)$$

$$W^\pm = \frac{(W_1 \mp iW_2)}{\sqrt{2}} \quad (1.2)$$

where θ_W , the mixing angle, is a parameter of the SM. Therefore, while γ is the force carrier for the electromagnetic force, the Z , W^+ , and W^- are the force carriers for the weak force. The weak interaction is interesting because it only acts on left-handed particles and right-handed anti-particles.

The vertexes describing the weak force interactions can be found in Figure 1.8. While the photon is massless, the three weak force carriers are not. The

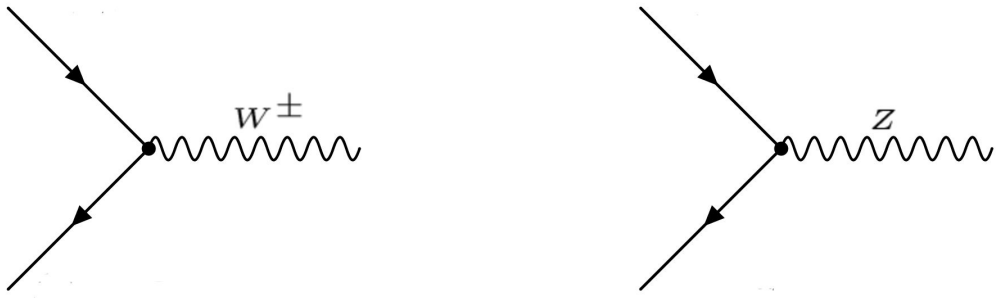


Figure 1.8: Weak interactions can be described by the following vertexes. The wavy lines represent bosons, while the straight lines represent any weak-interacting particle where the appropriate quantities are conserved.

Z boson has a mass of $91.2 \text{ GeV}/c^2$ (where protons have a mass of $\sim 1 \text{ GeV}/c^2$ for reference). The Z boson allows particles to interact with their anti-particles

through the weak force. For example, the process $Z \rightarrow e^-e^+$ is permitted, but the process $Z \rightarrow \mu^+e^-$ is not permitted. The Z boson can couple to both electrically-charged and -neutral particles, as well as particles with and without color.

The W^\pm boson, which has a mass of 80.4 GeV/c², also couples pairs of fermions. Rather than linking particles and anti-particles like the Z boson, it allows the flavors within a generation to interact. For example, a W^+ boson can decay to two quarks ($W^+ \rightarrow u\bar{d}$), and a W^- can decay to a lepton and its neutrino ($W^- \rightarrow \mu\nu_\mu$). Since the W^\pm is electrically charged, electric charge must be conserved at each vertex, and also $\gamma \rightarrow W^+W^-$ is allowed. The decay $Z \rightarrow W^+W^-$ is also a potential vertex.

The probability of a W decaying to different generations is dictated by the Cabibbo-Kobayashi-Maskawa (CKM) matrix, where each of these values has been experimentally measured:

$$\begin{pmatrix} V_{ud} & V_{us} & V_{ub} \\ V_{cd} & V_{cs} & V_{cb} \\ V_{td} & V_{ts} & V_{tb} \end{pmatrix} = \begin{pmatrix} 0.974 & 0.225 & 0.004 \\ 0.225 & 0.973 & 0.041 \\ 0.009 & 0.040 & 0.999 \end{pmatrix} \quad (1.3)$$

where $|V_{ij}|^2$ is the probability that a quark i decays to a quark j through the emission of a W.

Since all other particles decay through a W to a lighter particle, this explains why our world is built with the lightest two quarks (up and down quarks) and electrons, the building blocks of atoms.

1.1.7 Mass and the Higgs Boson

The Higgs Boson is the most recent confirmed Standard Model particle. It is related to the mass of other SM particles. To understand how this is so, we will look at the Higgs potential, which we can write as $V(\phi) \sim (\phi^2 - \eta^2)^2$ for the purpose of explanation. This is plotted in Figure 1.9. The potential

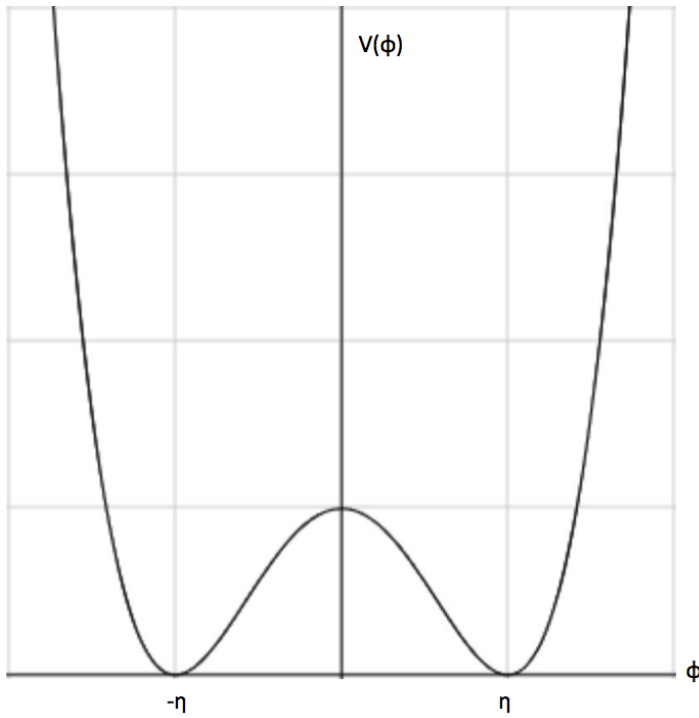


Figure 1.9: Approximation of the Higgs potential. While the shape is symmetric about the y-axis, the function is not symmetric about the minima.

is symmetric about the y-axis, or the axis with units of energy. In the early universe while everything was still very hot, the energies of particles were so high that the bumps at the bottom of the potential had no consequence. As the universe cooled, however, these minima became important, and one or the other minima was chosen. This is known as spontaneous symmetry breaking.

Once the universe had cooled sufficiently, the Higgs field took on a vacuum expectation value (VEV), or an average value in empty space, which was non-zero. This VEV couples to electroweak interactions, as referenced in the previous section, and the photon and weak force bosons mixed to form the states we know today. The spontaneously broken Higgs field also couples to itself, quarks, electrons, muons, taus, Z bosons, and W^\pm bosons. The magnitude of the coupling between the Higgs and a given particle determines the mass of the particle; the larger the coupling, the more massive the particle. However, it does not couple to neutrinos, so the explanation for their mass must lie elsewhere.

While we have been referring to the Higgs field, the Higgs boson is the particle that was recently discovered at the LHC in 2012. This particle is an excitation of the Higgs field in the same way that a photon is an excitation of the electromagnetic field. The SM Higgs has no charge, no spin, and a mass of 126 GeV. It couples to anything with mass (aside from the neutrinos), so it can also couple to itself. These vertexes take the form shown in Figure 1.10.

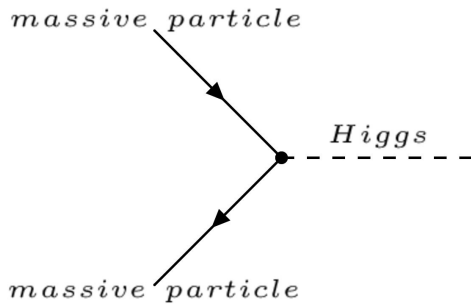


Figure 1.10: The Higgs Vertex. The dashed line is the Higgs Boson and the straight lines are any massive particle.

1.2 Rounding Up the Standard Model Particles

In total, including particles of different colors and all anti-particles, there exist 61 particles in the SM. We can describe their interactions easily using the vertices presented in each section. For example, consider the diagrams in Figure 1.11. These are important physics processes by which two gluons interact with

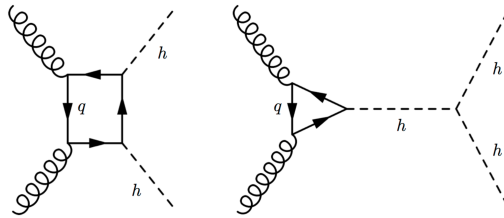


Figure 1.11: Left: Two gluons interact with a quark, while each gluon interacts with an additional different quark, and these additional different quarks interact with a shared fourth quark and each pair of quarks interacts to form a Higgs boson. Right: Two gluons interact with a quark, while each gluon interacts with an additional quark, and these additional different quarks interact with each other to form a Higgs boson, which interacts with two Higgs bosons. The result of both of these processes is a final state with two Higgs.

quarks to produce two Higgs, which is central to the topic of this thesis. This shows an example of the different kind of processes possible using Feynman diagrams: two protons collide and gluons inside of them interact with different quarks to produce two Higgs bosons (left) or one Higgs boson that then produces two Higgs bosons (right).

While this description has been qualitative, and has not drawn distinction between what has been experimentally determined and what has been predicted in the SM, the SM is quite self-consistent. There are only 19 parameters which are experimentally determined, most of which are masses.

1.3 Beyond the Standard Model

While the SM is an impressive feat of mathematics and experiments, it leaves many questions unanswered. For example, the SM only accounts for baryonic matter, which is estimated to be 4.6% of the universe. A remaining 24% is accounted for by dark matter, which can only be gravitationally detected, while the rest of the universe is said to be made up of dark energy.

The SM is also missing one of the four fundamental forces, gravity. While we have convincing understanding of quantum mechanics and general relativity, a unification for these two theories has yet to be discovered. Neutrino mass is unaccounted for by the SM. The Higgs mass is much lower than one might expect from the SM. The universe is dominated by matter, rather than anti-matter.

Many questions remain that require answers beyond the SM, and so we search for new particles and deviations in SM parameters at the LHC in hopes of providing new insight into these difficult problems.

Chapter 2

Introduction

2.1 Theoretical overview

The discovery of a boson with a mass of approximately 125 GeV, and with properties close to those expected for the Higgs boson (H) of the SM [3, 4], has stimulated interest in the exploration of the Higgs potential, described in 1. The production of a pair of Higgs bosons within the SM is a rare process that is sensitive to the structure of this potential through the self-coupling mechanism of the Higgs boson, as discussed in the previous chapter. An effective way to look for new physics is to examine the production cross section of two Higgs at the LHC.

A cross section tells us the probability of a particular final state of events. This depends on the initial conditions of the collision, or the energy going into the collision and what you are colliding. The unit used for cross section is barn, with $1\text{b} = 100\text{fm}^2 = 10^{-28}\text{m}^2$. In the SM, the cross section for the production of two Higgs bosons in pp collisions at 13 TeV is $33.5 \pm 2.5/2.8\text{ fb}$ for the gluon-gluon fusion process [5, 6, 7], which lies beyond the reach of analyses based on the first run of the CERN LHC. An increase in the cross section beyond

SM expectation would be a smoking gun for new physics. This can happen in one of two ways: there are new particles which decay to HH that contribute to the production of HH, or there are new processes, or additional vertices, that contribute to the production of HH. The first is called "resonant" production, since the increase in cross section is from a resonance (new particle), and the second is called "non-resonant", since it is a new Feynman diagram but not a new particle causing an increase in the cross section.

2.2 Resonant Production

Many theories beyond the SM (BSM) suggest different ways in which the cross section for the production of two Higgs would increase, based on the existence of heavy particles that can couple to a pair of Higgs bosons. Models with a warped extra dimension (WED), as proposed by Randall and Sundrum [8], postulate the existence of one spatial extra dimension compactified between two fixed points, commonly called branes. This would mean that in addition to our three spatial dimension and one temporal dimension, there exists a fifth dimension that's extremely small, such that it would be hard to observe this dimension. This fifth dimensional region between these two points, or branes, is often called the bulk. We define ϕ as the coordinate of this dimension, with the size parametrized by r_c , as can be seen in Figure 2.1. Then the metric for the full five-dimensional spacetime, which as it turns out solves Einstein's equations, can be written as

$$ds^2 = e^{-2kr_c\phi} \eta_{\mu\nu} dx^\mu dx^\nu + r_c^2 d\phi^2 \quad (2.1)$$

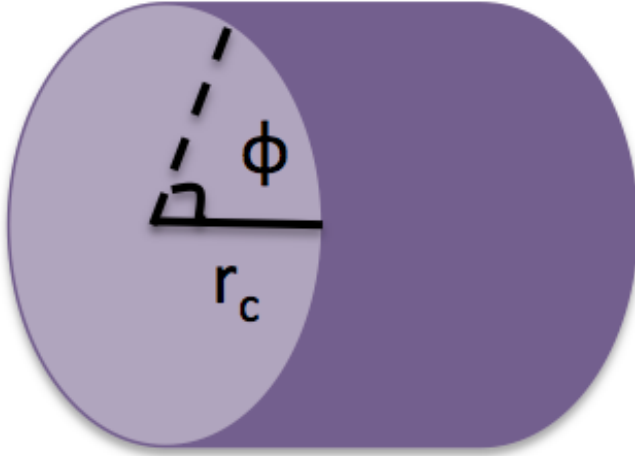


Figure 2.1: A depiction of the fifth extra dimension.

This means that four-dimensional mass scales (the masses we measure) are related to five-dimensional mass parameters (the masses predicted by the full five dimensional theory) by the warp factor, $e^{-2kr_c\phi}$. Therefore, this provides a good explanation as to why the Higgs boson mass is predicted to be on the order of the Planck scale ($M_{Pl} \sim 10^{18}$ GeV) but is observed to have a mass on the electroweak scale (125 GeV). This warp factor explains this relationship, without introducing a new hierarchy into the theory, since this large difference between the predicted and observed Higgs mass can be explained with a relatively small r_c . In this framework, we expect gravity to be much stronger in the bulk than in our four-dimensional world, which explains why gravity is observed to be so much weaker than the other three fundamental forces.

Lastly, this class of models predicts the existence of new particles. One of these particles would be the massless spin-2 graviton, which would give us insight into the inner workings of quantum gravity. There are also other new particles,

such as the spin-0 radion [9, 10, 11], and the spin-2 bulk graviton [12, 13, 14]. The radion is a particle that helps stabilize the size of the extra dimension. We consider the case where no mixing between the radion and Higgs boson (in other words, the two have separate mass states unrelated to each other). The couplings of SM particles to the bulk graviton depend on where SM particles can be located. In this analysis, we consider a scenario where SM particles are allowed in the bulk [15].

Supersymmetry is a class of theories that predict a supersymmetric new particle for every SM particle that currently exists. Some supersymmetric models also predict one spin-0 resonance that, when sufficiently massive, decays to a pair of SM Higgs bosons. Those would be additional Higgs bosons [16, 17]. The signal modeling for a spin-0 particle is identical if it is a radion or an additional Higgs boson.

In searching for the bulk graviton and radion, we will compare the cross section of di-Higgs production we observe in data to the cross sections predicted by these theories. If no new particles are found, then depending on the sensitivity of the analysis and the value of the cross section for bulk graviton and radion decay to di-Higgs, we may be able to rule out these particles below a certain mass. For the bulk graviton and radion signals that we consider, the tools used to calculate the cross sections for the production of KK graviton in the bulk and RS1 models are described in Ref. [18, 19]. The implementation of the calculations is described in Ref. [20].

Searches for narrow particles decaying to two Higgs bosons have already been performed by the ATLAS [21, 22, 23] and CMS [24, 25, 26] collaborations in pp collisions at $\sqrt{s} = 7$ and 8 TeV. Until now their reach was limited to $M_X =$

1.5 TeV. Moreover, some of the models that predict the coupling of the new resonance to HH also expect it to couple to W^+W^- or Z^0Z^0 [27]. Searches for these final states were performed by ATLAS and CMS [28, 29, 30, 31, 32].

2.3 Nonresonant Production

In the SM, non resonant pair production occurs primarily through gluon-gluon fusion via an internal fermion loop, which is dominated by the top quark, as can be seen in Figure 2.2. Assuming there are no new light states that we have

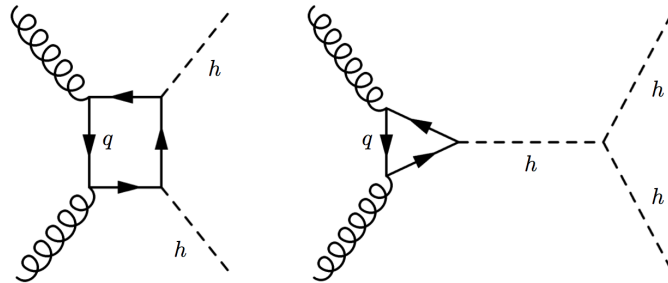


Figure 2.2: SM Feynman diagrams that contribute to Higgs boson pair production by gluon-gluon fusion at leading order.

not discovered yet, the gluon fusion Higgs boson pair production at the LHC can be described by five parameters, to leading order: κ_λ , κ_t , c_g , c_{2g} , and c_2 . The Higgs boson tri-linear coupling ($\lambda_{SM} = m_h^2/2v^2$, where v is the vacuum-expectation value of the Higgs field), and the top Yukawa interaction exist in the SM Lagrangian. Any deviations from the SM value for these two quantities is parametrized by κ_λ and κ_t , respectively. However, the interaction of Higgs and gluons, as well as two Higgs and two gluons or $t\bar{t}$, are not predicted by the

SM. These are instead parametrized by the absolute couplings c_g , c_{2g} , and c_2 .

We can then write out the Lagrangian describing all of these SM interactions and potential BSM interactions, assuming no other light states besides for SM particles, as an effective field theory:

$$\begin{aligned} \mathcal{L}_h = & \frac{1}{2}\partial_\mu h\partial^\mu h - \frac{1}{2}m_h^2 h^2 - \kappa_\lambda \lambda_{SM} v h^3 \\ & - \frac{m_t}{v}(v + \kappa_t h + \frac{c_2}{v} h h)(\bar{t}_L t_R + h.c.) + \frac{1}{4} \frac{\alpha_s}{3\pi v} (c_g h - \frac{c_{2g}}{2v} h h) G^{\mu\nu} G_{\mu\nu}, \end{aligned} \quad (2.2)$$

where the first two terms are the kinetic and mass term respectively for the Higgs, the third term is related to SM Higgs self-interactions (parametrized by κ_λ), the fourth term is related to both SM Higgs-top-antitop interactions (parametrized by κ_t) and BSM Higgs-Higgs-top-antitop interactions (parametrized by c_2), and the last term is related to BSM Higgs-gluon-gluon interactions (parameterized by c_g) and BSM Higgs-Higgs-gluon-gluon interactions (parameterized by c_{2g}). In the SM, $\kappa_\lambda=\kappa_t=1.0$ and the other three parameters are set to 0. The Feynman diagrams contributing to the di-Higgs signal at leading order can be found in Figure 2.3.

This shows that the phase space for the Higgs boson couplings in the BSM scenario has 5 parameters, where constraints come from measurements of single Higgs boson production and other theoretical considerations. For example, assuming electroweak symmetry is linearly realized, it turns out $c_{2g} = -c_g$ [33, 34]. While this phase space is large, the kinematics of di-Higgs production also depend on these five parameters. In particular, the distribution of the di-Higgs invariant mass and the modulus of the cosine of the polar angle of one Higgs boson with respect to the beam axis (modulus of the direction the protons come

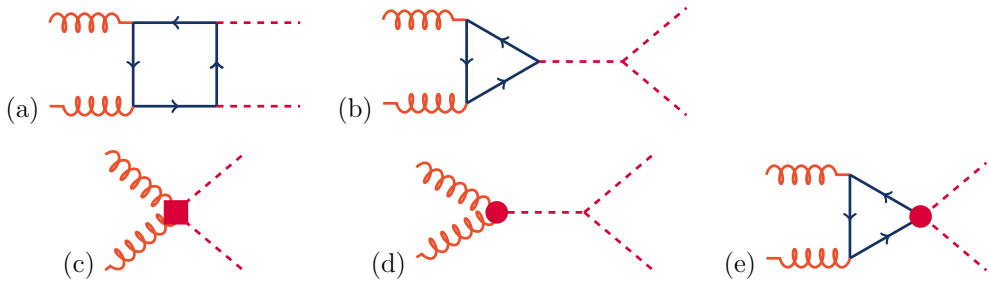


Figure 2.3: SM Feynman diagrams that contribute to Higgs boson pair production by gluon-gluon fusion at leading order. Diagrams (a) and (b) correspond to SM-like processes, while diagrams (c), (d), and (e) correspond to pure BSM effects: (c) and (d) describe contact interactions between the Higgs boson and gluons, and (e) exploits the contact interaction of two Higgs bosons with top quarks.

from), are similar across many different parameter combinations. A statistical approach was developed to identify twelve clusters of models with similar distribution in both kinematic variables, described in full in Reference [35]. Twelve benchmarks, one from each cluster, were chosen to represent the model that best represents each cluster. These are described in Table 2.1, along with the SM values of the parameters. The invariant mass distributions of the twelve BSM scenarios can be found in Figure 2.4, while the modulus of the cosine of the polar angle of one Higgs boson with respect to the beam axis ($|\cos\theta^*|$) can be found in Figure 2.5.

There is still much to be learned about the Higgs boson, the potential of the Higgs field, and other properties related to the Higgs. In particular, probing the Higgs potential by examining non-resonant production of di-Higgs is one of the most important tasks that the next generation LHC will tackle. While we don't

Benchmark	κ_λ	κ_t	c_2	c_g	c_{2g}
1	7.5	1.0	-1.0	0.0	0.0
2	1.0	1.0	0.5	-0.8	0.6
3	1.0	1.0	-1.5	0.0	-0.8
4	-3.5	1.5	-3.0	0.0	0.0
5	1.0	1.0	0.0	0.8	-1.0
6	2.4	1.0	0.0	0.2	-0.2
7	5.0	1.0	0.0	0.2	-0.2
8	15.0	1.0	0.0	-1.0	1.0
9	1.0	1.0	1.0	-0.6	0.6
10	10.0	1.5	-1.0	0.0	0.0
11	2.4	1.0	0.0	1.0	-1.0
12	15.0	1.0	1.0	0.0	0.0
SM	1.0	1.0	0.0	0.0	0.0

Table 2.1: Parameter values of the final benchmarks selected with number of clusters $N_{clus} = 12$.

currently have enough sensitivity to effectively probe the Higgs potential, we are able to test out strategies to find the best way to probe the Higgs potential in the future.

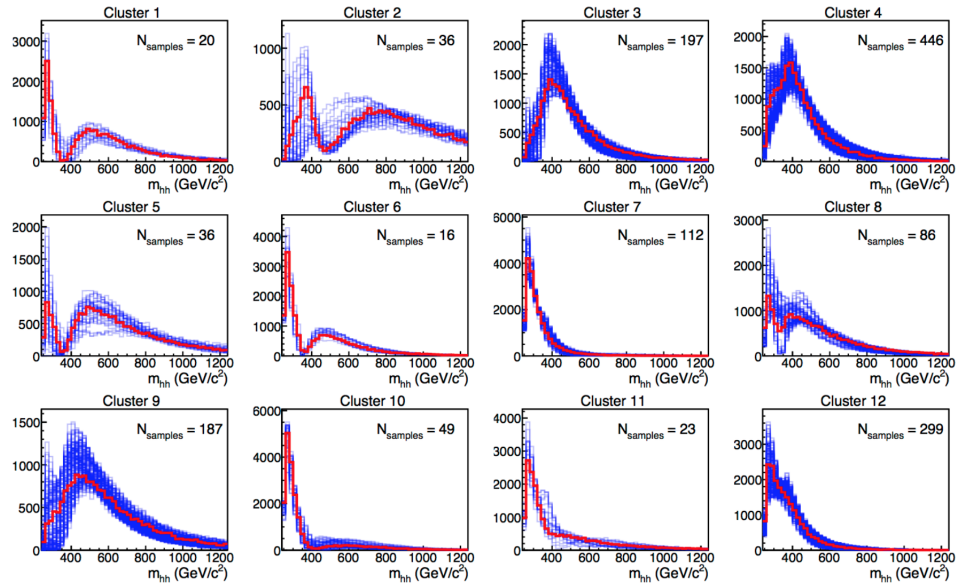


Figure 2.4: The invariant mass of the two Higgs for Monte Carlo simulation of different parameter combinations, clustered into 12 classes of shapes. The red distributions correspond to the benchmark model, while the blue distributions are the other parameter combinations similar to the benchmark that are part of that cluster.

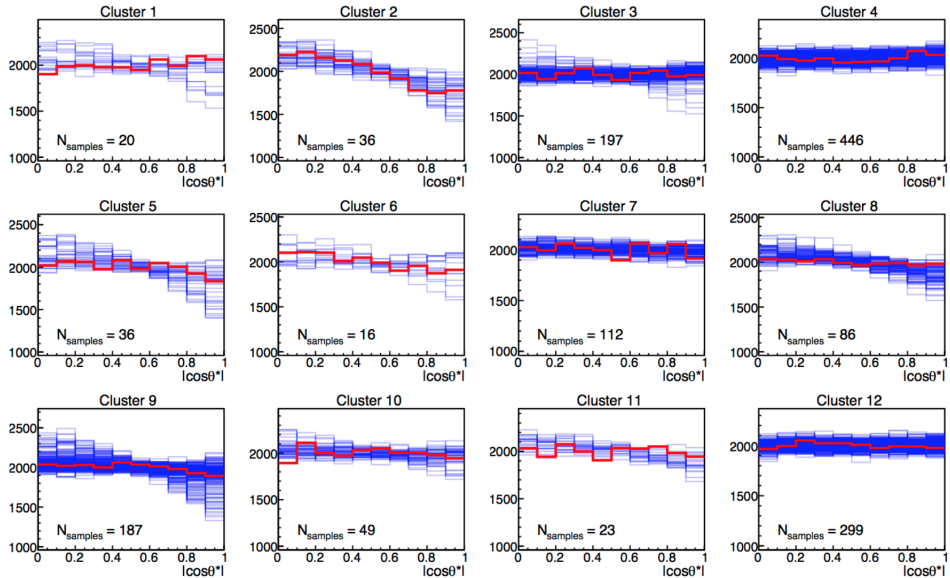


Figure 2.5: The modulus of the cosine of the polar angle of one Higgs boson with respect to the beam axis for Monte Carlo simulation of different parameter combinations, clustered into 12 classes of shapes. The red distributions correspond to the benchmark model, while the blue distributions are the other parameter combinations similar to the benchmark that are part of that cluster.

Chapter 3

Searching for New Particles

One of the most effective ways to probe the SM further and have a chance at discovering new BSM particles is to smash SM particles together at high energies in hopes of discovering something new. One of the easiest colliders to imagine is an electron-positron collider. Such colliders have existed over the past century and the experiments performed there account for many precision SM measurements. High energy collisions allow for a greater chance of something new and massive appearing, and allow for more precise measurements. However, it is hard to produce high energy collisions with electrons and positrons. Charged particles radiate energy when they are traveling through an electromagnetic field, where the power radiated is given by

$$P = \frac{e^4}{6\pi m^4 c^5} E^2 B^2 \quad (3.1)$$

Due to the low mass of electrons and positrons, they radiate much more energy than a heavier particle would. In order to reach high energies, then, colliding protons provides the most effective solution to date, and this is exactly what the Large Hadron Collider at CERN was built to do.

3.1 The Large Hadron Collider

The Large Hadron Collider (LHC) [36] is the largest collider ever built, colliding protons at the highest energy produced inside a collider, and producing more data than all other experiments combined. The LHC is located in a tunnel 100m underground on the border of Switzerland and France at CERN (European Center for Nuclear Research), near Geneva, Switzerland. It has been running since 2007, colliding protons at a center of mass energy 7 TeV from 2007-2011, 8 TeV from 2011-2015, and now at 13 TeV.

In order to create the proton beams used for collision in the LHC, the energy of the protons used for collisions is ramped up slowly. Hydrogen is stripped of electrons and fed into a linear accelerator, and then a succession of increasingly large circular synchrotrons. A schematic of the LHC and the smaller accelerators that feed into the main ring can be found in Figure 3.1, along with an aerial view of CERN. Once the two beams of protons enter the LHC, they are accelerated to

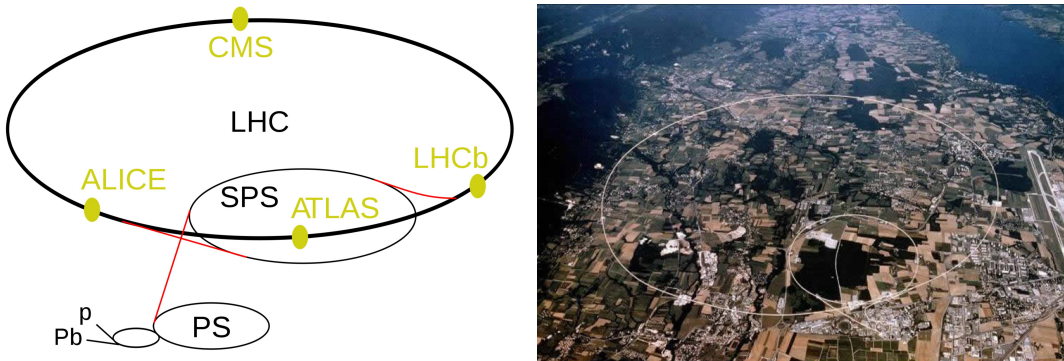


Figure 3.1: (left) Schematic of the LHC and the smaller accelerators which feed into the LHC. (right) Aerial view of Geneva. The larger circle marks the location of the LHC, safely underneath the ground.

collision energies (currently 13 TeV, or 6.5 TeV per beam). These beams travel

in opposite directions around the ring, which contains 1,232 dipole magnets to direct and accelerate the beams and 392 quadrupole magnets to focus the beams. The superconducting magnets are cooled to less than 2K and produce a 7T field. The protons travel in bunches of roughly 115 billion each, with a spacing of 25 nanoseconds between crossings, barreling along at 99.9999999% the speed of light to collide within four detectors: ALICE, ATLAS, CMS, and LHCb.

3.1.1 A proton-proton Collision

Because protons are composite particles, their collisions are not simple. While we speak of protons as being comprised of two up quarks and one down quark, these are only the valence quarks of the proton. The inner-workings of a proton are actually a complicated, ongoing interaction between these three valence quarks, where this interaction involves gluons. These gluons also interact with each other, spontaneously producing different quarks which interact to become gluons again. Therefore, when protons are collided at the energy scales of a machine such as the LHC, we are actually colliding quarks and gluons, rather than protons. We call these quarks and gluons partons.

This makes it much more difficult to know what is actually interacting in each collision. We rely on Parton Distribution Functions [37, 38] for a statistical understanding of what may be happening. Figure 3.2 shows two different simulated PDF sets. The x-axis represents the fraction of energy of the proton that belongs to a particular parton, while the y-axis tells us the probability of a particular parton having this particular energy. The various curves represent

different partons, where the subscript "v" indicates a valence quark. The left plot shows a low energy scale, while the right plot is for the LHC energy scale. For example, at the LHC scale, there is a $\sim 50\%$ probability that an up valence quark is carrying 10% of the proton's energy. It is of interest to note that at

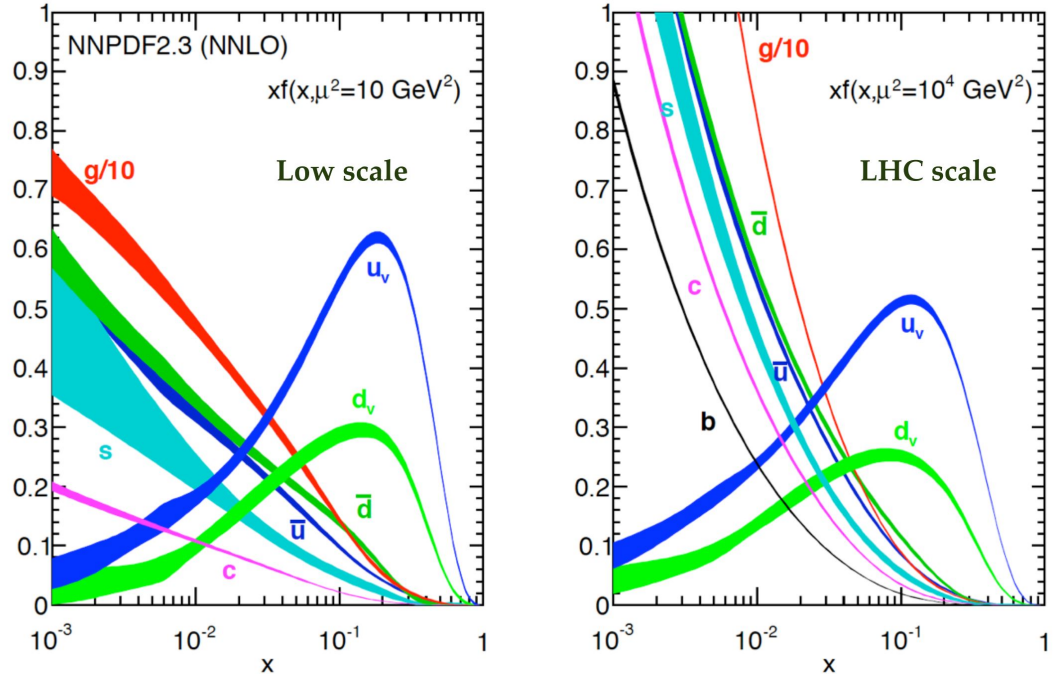


Figure 3.2: PDF for 10 GeV (left) and 10 TeV (right) collisions. Each curve represents a parton in a proton, and tells us the probability (y-axis) of finding that parton carrying momentum fraction x of the total momentum of the proton.

higher energies, gluon-gluon or quark-gluon interactions occur more often than they do at lower energies. It is important to have correct PDFs to predict the amount of new physics one might see at the LHC. For example, the non-resonant production considered in this thesis is only through gluon-gluon interactions, so this must be taken into account when producing simulated signal events. Unfortunately, it is hard to compute PDFs, so in order to have the best possible idea of what PDFs look like, partial models are combined with many measurements

performed at fixed target and collider experiments to get more accurate values. There is a systematic uncertainty associated with this process which will be discussed in more detail in later chapters.

3.2 The Compact Muon Solenoid

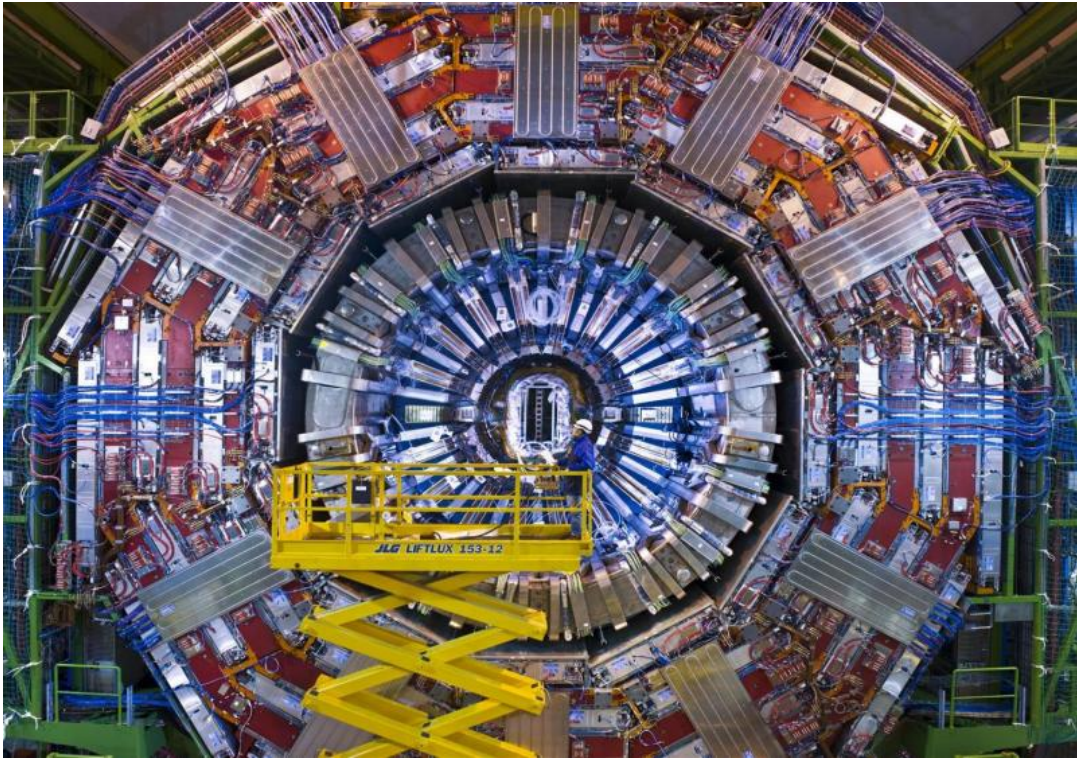


Figure 3.3: The Compact Muon Solenoid detector.

In order to make use of these proton-proton collisions, a carefully designed detector is necessary to capture the data. There are two general purpose detectors on the LHC, which serve to look for new physics and test current SM predictions. The analysis presented in this thesis was performed on data taken with one of these two detectors: the Compact Muon Solenoid (CMS)[39], as

can be seen in Figure 3.3. Armed with a team of roughly 4,000 scientists, this five-story, 14,000 ton piece of hardware has been the subject of many previous theses and papers. A brief overview is presented here so as to give context to the data analysis performed in this thesis. A slice of the detector is sketched in Figure 3.4; each component will be described in the following sections to build an understanding of the detector as a whole.

3.2.1 Coordinates

The CMS detector geometry approximates that of a large cylinder, with detectors in the barrel of the cylinder and at either end (endcaps). Coordinates in the detector are defined as shown in Figure 3.5. The z-axis is parallel to the beam line; protons come in from the +z-axis and -z-axis. The y-axis points directly up and the x-axis points directly sideways. The azimuthal angle ϕ is in reference to the x-axis, where $\phi = 0$ is along the x-axis. The polar angle θ is parametrized in terms of pseudorapidity η , where

$$\eta = -\ln \left(\tan \frac{\theta}{2} \right) \quad (3.2)$$

We use η instead of θ because pseudorapidity is a Lorentz-invariant quantity, meaning that it is the same in any Lorentz frame. This is critical for any quantity measured with respect to the beam line, since partons may not be symmetric in the laboratory rest frame because they may carry different fractions of energy of their respective protons.

Three quantities are recorded for each particle passing through the CMS detector: azimuthal angle ϕ , pseudorapidity η , and transverse momentum p_T ,

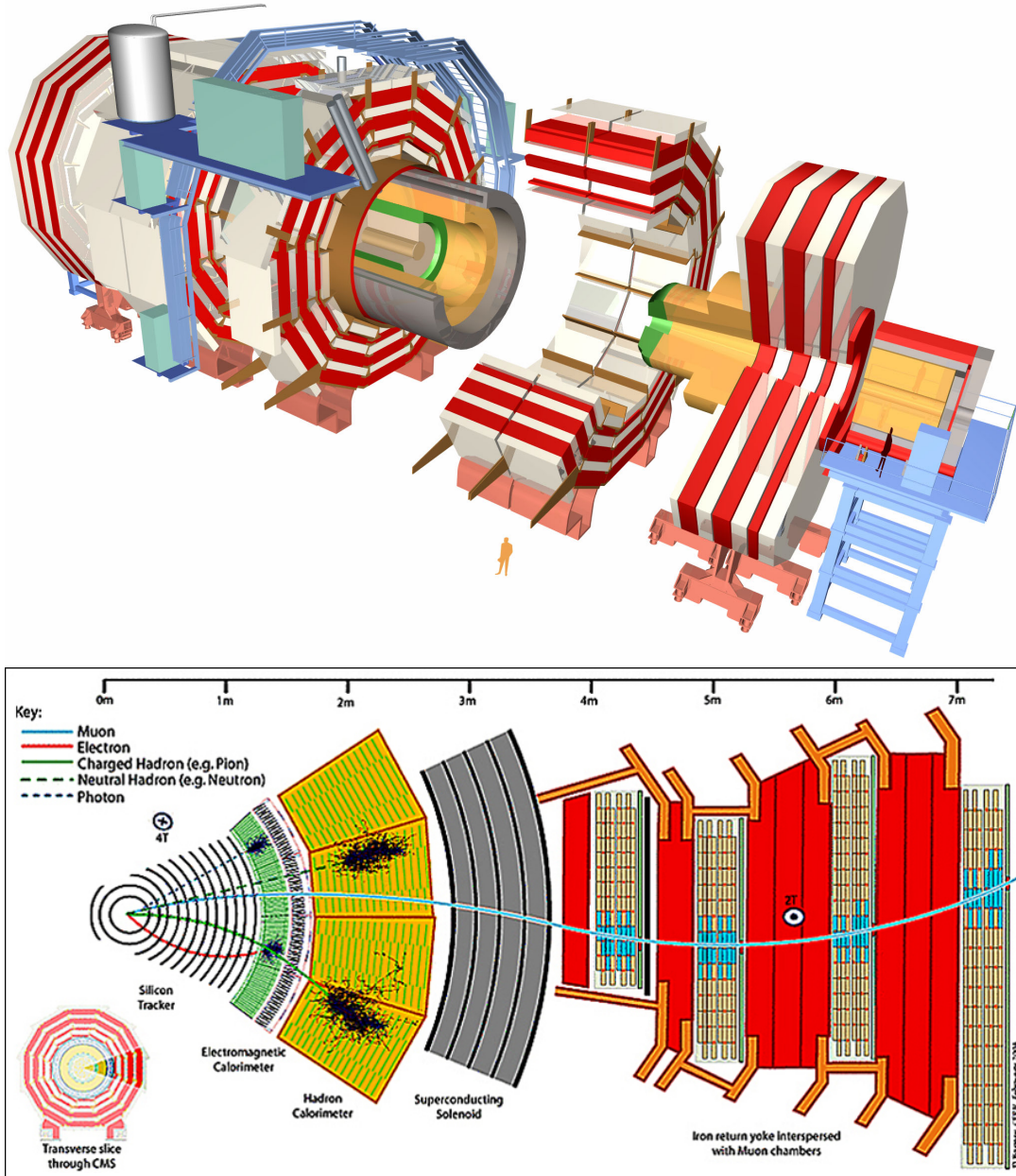


Figure 3.4: CMS detector with a person for size (top). Slice of the CMS detector, depicting the different components and the signatures of some of the different particles that pass through the detector after a proton-proton collision occurs (bottom).

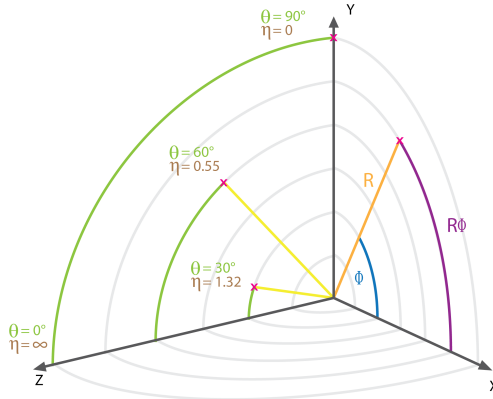


Figure 3.5: Coordinates of the CMS detector.

defined as $p_T = \sqrt{p_X^2 + p_Y^2}$, or the momentum in the plane transverse to the beam line. Transverse momentum is used rather than momentum because the initial state of collisions has $p_T = 0$, while p_Z is hard to determine. Momentum in Cartesian coordinates can be calculated with the following transformations,

$$p_X = p_T \cos \phi, \quad p_Y = p_T \sin \phi, \quad p_Z = p_T \cosh \eta, \quad (3.3)$$

although this is rarely necessary.

3.2.2 The Tracker

The innermost layer of the detector is a tracker made out of silicon. The tracker records the paths of charged particles as they pass through. It has 13 layers in the barrel, and 14 in the endcaps. The first four layers are made up of silicon pixels, while the remaining layers are strips. Each pixel is $100 \times 150 \mu\text{m}$ in area, while each strip is $180 \mu\text{m}$ by 10 cm or 25 cm, depending on where the strip is located. While this adds up to over 200 m^2 of silicon sensors, the detector itself

is not much larger than a shoe box.

Charged particles passing through the detector interact with the silicon to produce "hits" which allows us to determine a particle's location to within $10\mu\text{m}$. Because the tracker is inside a strong magnetic field (described below), the tracks of these charged particles bend. This allows us to make a measurement on the charge and momentum of the particle; the higher momentum the particle, the less curved the track.

3.2.3 The Calorimeters

The electromagnetic calorimeter is next to the tracker, followed by the hadronic calorimeter. While the purpose of a tracker is to allow a particle to pass through the detector in order to record the full track of a particle, the purpose of a calorimeter is to stop a particle so that a full measurement of the particle's energy can be obtained. Unlike the tracker, both charged and neutral particles interact with the calorimeter.

The electromagnetic calorimeter (ECAL) is built to measure the energy deposited by electrons, positrons, and photons. It is made of $\sim 80,000$ lead-tungstate (PbWO_4) crystals. Lead-tungstate crystal emits light, or scintillates, when particles deposit energy in the compound. It was chosen for its short radiation length and short Moliere length, both of which force particles to stop faster, allowing for a compact ECAL. By measuring the light produced by a particle in the ECAL, we can measure the energy of the particle. Particles heavier than an electron or photon continue on through the detector to be measured by the hadronic calorimeter.

The hadronic calorimeter (HCAL) is built to measure the energy deposited by hadrons. It is comprised of layers of an absorber, which causes an electromagnetic shower when a particle deposits energy, alternated with layers of an active medium, which measures the light emitted in the electromagnetic shower. The absorber chosen for the HCAL is brass, made out of Russian naval shells recycled from WW2, and chosen for its short interaction length (once again allowing for a more compact detector) and because brass is non-magnetic. The active medium is a plastic scintillator, which allows us to measure the amount of light caused by both charged and neutral hadron interactions with the brass, and therefore allows us to measure the energy of these particles.

3.2.4 The Solenoid

By choosing the material for the inner three components carefully, the CMS design allows for all three of these detectors to fit within a large solenoid magnet (hence "**Compact Muon Solenoid**", which produces a 3.8 Tesla magnetic field. This field causes the tracks of charged particles to bend within the inner three detectors, allowing us to make momentum measurements from tracks in the tracker.

3.2.5 The Muon Chambers

The last and largest component of the detector is the muon chambers. It is designed to measure the location, momentum, and energy of muons, which are too heavy to be stopped by the ECAL but not heavy enough to be stopped by the HCAL. This detector is comprised of three different types of detectors

(drift tube chambers, cathode strip chambers, resistive plate chambers), all of which operate on the same principle: as the muon travels through the detector, it knocks electrons off of gas atoms, which are then collected to measure the energy and location of the muon. These detectors are alternated with layers of steel, which stop non-muons from passing through. These layers also direct and contain the weak magnetic field outside of the solenoid, which allows for a precise momentum measurement of the muon (hence "Compact **Muon** Solenoid"). This is done by measuring the muon's curvature both in the tracker and in the muon chambers (it curves opposite directions in each of these, as can be seen in Figure 3.4).

3.2.6 What's Missing?

Some particles, such as neutrinos, are so weakly interacting that they pass right through the detector. We would potentially expect the same from some BSM particles, such as dark matter. However, because of the law of conservation of energy, we can infer a direction and magnitude for these missing particle(s). In the x and y direction, or the transverse plane, which is perpendicular to the beam line, the initial state condition requires that total momentum is 0, where all of the momentum is in the z-direction (Figure 3.6, top). Having measured all particles that are registered by the detector carefully after the collision, with detectors that leave very little space uncovered for a particle to slip through, we are then able to reconstruct whether there is any missing energy in the transverse plane based off of energy conservation laws (Figure 3.6, bottom). While we can't say anything definitive about what particle(s) is(are) missing,

we can report the total missing transverse momentum p_T and the azimuthal angle (ϕ) associated with this missing energy.

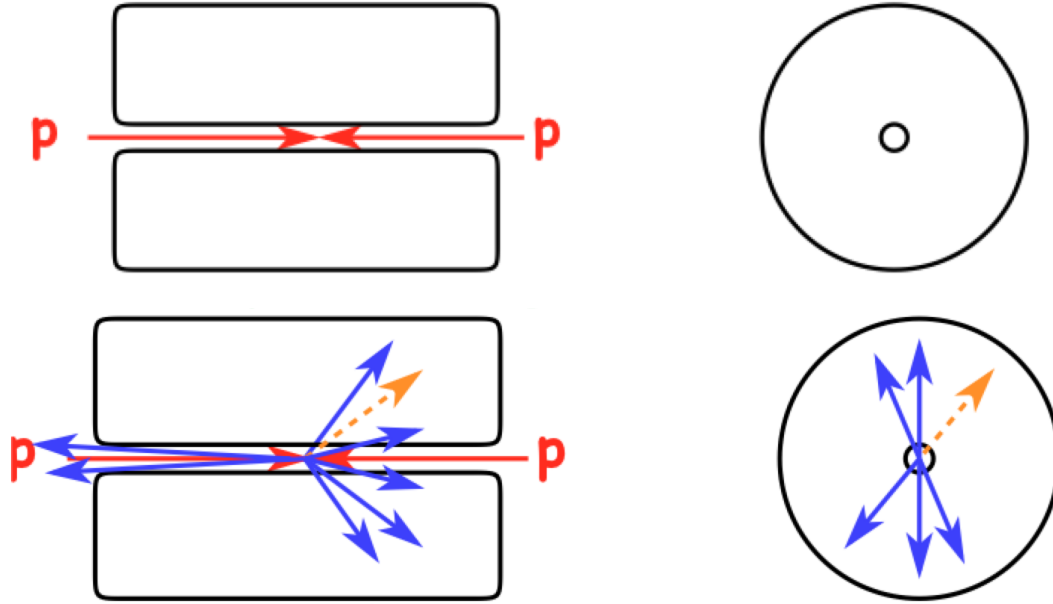


Figure 3.6: Diagram of particles inside the detector pre-collision (top) and post-collision (bottom), where post-collision shows where the protons entered, which particles were recorded (blue), and the direction of the missing energy (orange).

3.2.7 The Particle Flow Algorithm

Information from all of the detectors is collected and analyzed by the Particle Flow Algorithm (PF Algorithm, or PF) [40], which allows for an accurate event by event reconstruction by combining information from detectors, rather than treating the information separately.

3.2.8 Jets

As mentioned in Chapter 1, all particles that exist in nature must be color-neutral. When proton-proton collision result in bare quarks or gluon, the process of hadronization begins immediately, and new quarks are produced from the vacuum until it is no longer energetically favorable. This creates a spray of hadronic activity; wherever one quark or gluon is, many more will exist in a conical structure that points in the direction the original quark or gluon was moving. A depiction of these in a real event at the LHC is shown in Figure 3.7, where the yellow cones represent these hadronic showers, which are called jets. Jets are

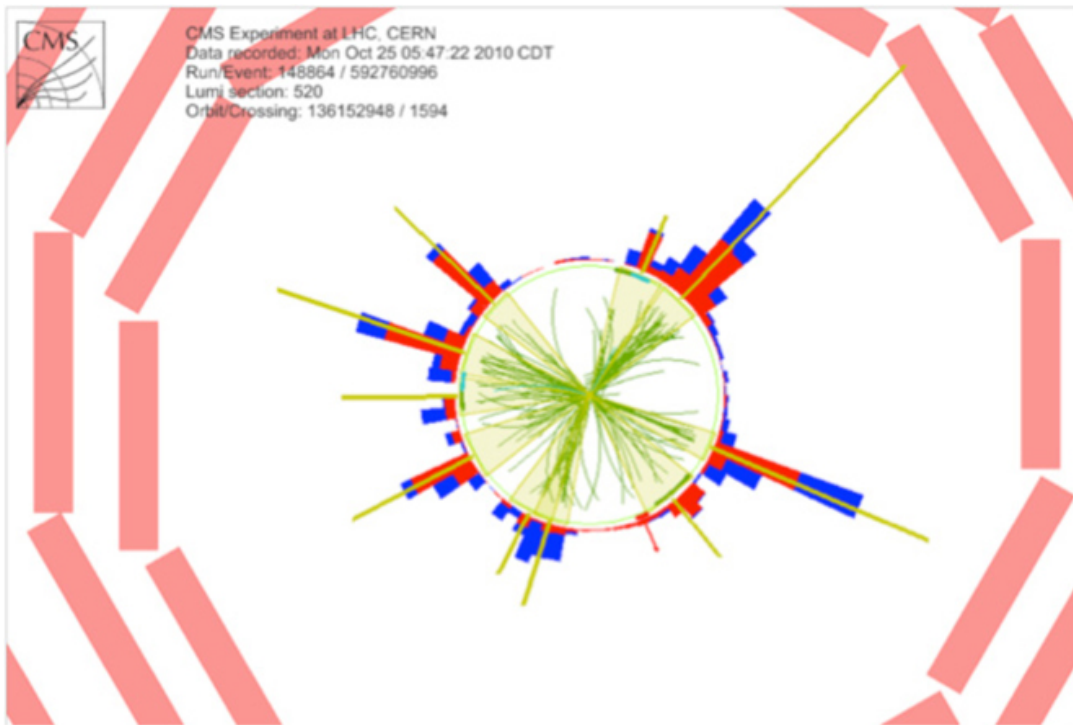


Figure 3.7: Typical CMS event with large number of hadrons (tracks represented by green lines, HCAL energy in blue, ECAL energy in red). These hadrons are collected into *jets* (shown by yellow triangles). The PF algorithm combines information from the trackers and calorimeters to properly measure the total momentum and energy of the jet.

composed of constituents which are defined by combining tracker, calorimeter, and muon system information from the PF Algorithm. These constituents are clustered into jets, making educated guesses as to which constituents belong to which jets. A number of algorithms exist for clustering, but the jets used in this analysis are clustered with the anti- K_T algorithm [41]. Using this method, every PF candidate, or particle reconstructed with the PF Algorithm, is compared with all of the other candidates, measuring a distance-like parameter between each pair. The two closest constituents are paired to become a new constituent. This process continues until the distance-like parameter between the jet and the beam is equal to $1/p_T^2$ of this new conglomerate constituent. Then this constituent is considered a jet and is removed from consideration. This continues until no constituents remain.

The anti- K_T algorithm tends to produce conical jets with smooth, rounded edges. Jets of this type are referred to as AKR jets, where R is the radius of the jet. Two types of jet are used in this analysis: AK8 and AK4, with R=0.8 and R=0.4 respectively, depending on how collimated we expect decay products to be.

3.2.9 Triggers

The detector output from each collision would require roughly a megabyte of space to store. Given that roughly 600 million collisions happen per second, there is no way to store all of the data. In fact, over 99% of data is thrown out, and only the interesting events are kept. The trigger system is responsible for determining which events matter, and which do not.

There are two stages of the trigger system. The Level 1 Trigger is comprised of hardware. Detector output is temporarily stored and analyzed to look for "interesting" physics, such as large amounts of HCAL energy or a high energy muon. This stage removes 99% of collisions, passing the remaining events to the next stage.

The High Level Trigger (HLT), comprised of software, analyzes the output of the Level 1 trigger. Events are reconstructed more fully and sorted into different categories should they pass the HLT criteria. Any remaining events that do not pass selection are discarded. Different HLT paths are associated with different interesting physics. For example, events with a muon with $p_T > 50$ GeV would pass the *HLT_Mu50* trigger while events with total transverse energy, known as H_T , larger than 800 would pass the *HLT_HT800*. If an event passes both criteria, then it passes both triggers. Most triggers retain all events passing the required criteria for that particular trigger, but some triggers, called prescale triggers, pass only a fraction of the events that pass the criteria. These triggers tend to have looser criteria and are designed to be used for measuring the efficiency of unprescaled triggers for a given analysis. The comparison of this efficiency measurement in data and simulation plays an important role in systematics, which will be discussed in later chapters.

3.2.10 Pileup

While we tend to speak of collisions at the LHC as a clean event, in which two protons enter the detector and collide, this is not entirely accurate. The protons come in bunches, and therefore, multiple protons can collide in the same event.

Some events can even contain up to forty individual interactions. Because of this, we define a primary vertex for the event, which is a point along the beam line from which the highest value of the sum of square of the p_T of Particle Flow objects originate.

Pileup, or the rest of the event aside from the interaction originating from this primary vertex, can affect the algorithms for creating jets. We account for the effects of pileup on jet related quantities such as mass in the evaluation of systematics, discussed in later chapters.

Bibliography

- [1] CERN, “Go on a Particle Quest at the First CERN Webfest,”
<https://cds.cern.ch/journal/CERNBulletin/2012/35/News%20Articles/1473657>,
2012.
- [2] “Preliminary communications on electric discharges in rarefied gases,”
Monatsberichte der Kauniglich Preussischen Akademie der Wissenschaften
zu Berlin, p. 286, 1876.
- [3] S. Chatrchyan *et al.*, “Observation of a new boson at a mass of 125 GeV
with the CMS experiment at the LHC,” *Phys. Lett. B*, vol. 716, p. 30, 2012.
- [4] G. Aad *et al.*, “Observation of a new particle in the search for the Standard
Model Higgs boson with the ATLAS detector at the LHC,” *Phys. Lett. B*,
vol. 716, p. 1, 2012.
- [5] D. de Florian *et al.*, “Handbook of LHC Higgs cross sections: 4. deciphering
the nature of the Higgs sector,” CERN, CERN Report CERN-2017-002-M,
2016.
- [6] D. de Florian and J. Mazzitelli, “Higgs Boson Pair Production at Next-
to-Next-to-Leading Order in QCD,” *Phys. Rev. Lett.*, vol. 111, p. 201801,
2013.

- [7] J. Baglio, A. Djouadi, R. GrÃüber, M. M. MÃijhlleitner, J. Quevillon, and M. Spira, “The measurement of the Higgs self-coupling at the LHC: theoretical status,” *JHEP*, vol. 04, p. 151, 2013.
- [8] L. Randall and R. Sundrum, “A large mass hierarchy from a small extra dimension,” *Phys. Rev. Lett.*, vol. 83, p. 3370, 1999.
- [9] W. D. Goldberger and M. B. Wise, “Modulus stabilization with bulk fields,” *Phys. Rev. Lett.*, vol. 83, p. 4922, 1999.
- [10] O. DeWolfe, D. Z. Freedman, S. S. Gubser, and A. Karch, “Modeling the fifth dimension with scalars and gravity,” *Phys. Rev. D*, vol. 62, p. 046008, 2000.
- [11] C. Csaki, M. Graesser, L. Randall, and J. Terning, “Cosmology of brane models with radion stabilization,” *Phys. Rev. D*, vol. 62, p. 045015, 2000.
- [12] H. Davoudiasl, J. L. Hewett, and T. G. Rizzo, “Phenomenology of the Randall-Sundrum Gauge Hierarchy Model,” *Phys. Rev. Lett.*, vol. 84, p. 2080, 2000.
- [13] C. Csaki, M. L. Graesser, and G. D. Kribs, “Radion dynamics and electroweak physics,” *Phys. Rev. D*, vol. 63, p. 065002, 2001.
- [14] K. Agashe, H. Davoudiasl, G. Perez, and A. Soni, “Warped Gravitons at the LHC and Beyond,” *Phys. Rev. D*, vol. 76, p. 036006, 2007.
- [15] A. L. Fitzpatrick, J. Kaplan, L. Randall, and L.-T. Wang, “Searching for the Kaluza-Klein Graviton in Bulk RS Models,” *JHEP*, vol. 09, p. 013, 2007.

- [16] A. Djouadi, “The anatomy of electroweak symmetry breaking. Tome II: the Higgs bosons in the minimal supersymmetric model,” *Phys. Rept.*, vol. 459, p. 1, 2008.
- [17] R. Barbieri, D. Buttazzo, K. Kannike, F. Sala, and A. Tesi, “One or more Higgs bosons?” *Phys. Rev. D*, vol. 88, p. 055011, 2013.
- [18] K. Agashe, O. Antipin *et al.*, “Warped Extra Dimensional Benchmarks for Snowmass 2013,” in *Community Summer Study 2013: Snowmass on the Mississippi (CSS2013) Minneapolis, MN, USA, July 29-August 6, 2013*, 2013. [Online]. Available: <http://cp3-origins.dk/research/units/ed-tools>
- [19] P. de Aquino, K. Hagiwara, Q. Li, and F. Maltoni, “Simulating graviton production at hadron colliders,” *JHEP*, vol. 06, p. 132, 2011. [Online]. Available: <http://feynrules.irmp.ucl.ac.be/wiki/RSmodel>
- [20] A. Oliveira, “Gravity particles from Warped Extra Dimensions, a review. Part I - KK Graviton,” 2014, submitted on arXiv.
- [21] G. Aad *et al.*, “Search For Higgs Boson Pair Production in the $\gamma\gamma b\bar{b}$ Final State using pp Collision Data at $\sqrt{s} = 8$ TeV from the ATLAS Detector,” *Phys. Rev. Lett.*, vol. 114, p. 081802, 2015.
- [22] ———, “Search for Higgs boson pair production in the $b\bar{b}b\bar{b}$ final state from pp collisions at $\sqrt{s} = 8$ TeV with the ATLAS detector,” *Eur. Phys. J. C*, vol. 75, p. 412, 2015.

- [23] ——, “Searches for Higgs boson pair production in the $hh \rightarrow bb\tau\tau, \gamma\gamma WW^*, \gamma\gamma bb, bbbb$ channels with the ATLAS detector,” *Phys. Rev. D*, vol. 92, p. 092004, 2015.
- [24] V. Khachatryan *et al.*, “Searches for heavy Higgs bosons in two-Higgs-doublet models and for $t \rightarrow ch$ decay using multilepton and diphoton final states in pp collisions at 8 TeV,” *Phys. Rev. D*, vol. 90, p. 112013, 2014.
- [25] ——, “Search for resonant pair production of Higgs bosons decaying to two bottom quark-antiquark pairs in proton-proton collisions at 8 TeV,” *Phys. Lett. B*, vol. 749, p. 560, 2015.
- [26] ——, “Searches for a heavy scalar boson H decaying to a pair of 125 GeV Higgs bosons hh or for a heavy pseudoscalar boson A decaying to Zh , in the final states with $h \rightarrow \tau\tau$,” *Phys. Lett. B*, vol. 755, pp. 217–244, 2016.
- [27] J. Brehmer *et al.*, “The Diboson Excess: Experimental Situation and Classification of Explanations; A Les Houches Pre-Proceeding,” 2015, submitted on arXiv.
- [28] G. Aad *et al.*, “Search for high-mass diboson resonances with boson-tagged jets in proton-proton collisions at $\sqrt{s} = 8$ TeV with the ATLAS detector,” *JHEP*, vol. 12, p. 055, 2015.
- [29] ——, “Search for production of WW/WZ resonances decaying to a lepton, neutrino and jets in pp collisions at $\sqrt{s} = 8$ TeV with the ATLAS detector,” *Eur. Phys. J. C*, vol. 75, p. 209, 2015, [Erratum: 10.1140/epjc/s10052-015-3593-4].

- [30] ——, “Search for resonant diboson production in the $\ell\ell q\bar{q}$ final state in pp collisions at $\sqrt{s} = 8$ TeV with the ATLAS detector,” *Eur. Phys. J. C*, vol. 75, p. 69, 2015.
- [31] V. Khachatryan *et al.*, “Search for massive resonances in dijet systems containing jets tagged as W or Z boson decays in pp collisions at $\sqrt{s} = 8$ TeV,” *JHEP*, vol. 08, p. 173, 2014.
- [32] ——, “Search for massive resonances decaying into pairs of boosted bosons in semi-leptonic final states at $\sqrt{s} = 8$ TeV,” *JHEP*, vol. 08, p. 174, 2014.
- [33] G. F. Giudice, C. Grojean, A. Pomarol, and R. Rattazzi, “The Strongly-Interacting Light Higgs,” *JHEP*, vol. 06, p. 045, 2007.
- [34] W. BuchmÃjller and D. Wyler, “Effective lagrangian analysis of new interactions and flavour conservation,” *Nuclear Physics B*, vol. 268, no. 3, pp. 621 – 653, 1986. [Online]. Available: <http://www.sciencedirect.com/science/article/pii/0550321386902622>
- [35] A. Carvalho, M. Dall’Osso, T. Dorigo, F. Goertz, C. A. Gottardo, and M. Tosi, “Higgs pair production: choosing benchmarks with cluster analysis,” *Journal of High Energy Physics*, vol. 2016, no. 4, p. 126, Apr 2016. [Online]. Available: [https://doi.org/10.1007/JHEP04\(2016\)126](https://doi.org/10.1007/JHEP04(2016)126)
- [36] “Lhc the guide,” <http://cds.cern.ch/record/1092437/files/CERN-Brochure-2008-001-Eng.pdf>.
- [37] D. Bourilkov, R. C. Group, and M. R. Whalley, “LHAPDF: PDF use from the Tevatron to the LHC,” 2006.

- [38] R. D. Ball *et al.*, “Parton distributions for the LHC Run II,” *JHEP*, vol. 04, p. 040, 2015.
- [39] S. Chatrchyan *et al.*, *CMS Physics: Technical Design Report Volume 1: Detector Performance and Software*, ser. Technical Design Report CMS. Geneva: CERN, 2006, there is an error on cover due to a technical problem for some items.
- [40] CMS Collaboration, “Particle-flow event reconstruction in CMS and performance for jets, taus, and ,” CMS Physics Analysis Summary CMS-PAS-PFT-09-001, 2009. [Online]. Available: <http://cdsweb.cern.ch/record/1194487>
- [41] M. Cacciari, G. P. Salam, and G. Soyez, “The anti- k_t jet clustering algorithm,” *JHEP*, vol. 04, p. 063, 2008.